**Title:** Impact of Equilibrative Nucleoside Transporters on *Toxoplasma gondii* Infection and Differentiation.

Gabriel Messina[1], Amber Goerner[1] Charlotte Bennett[1], Euwen Brennan[1], Vern B. Carruthers[2], Bruno Martorelli Di Genova[1*]

[1] – Department of Microbiology and Molecular Genetics, University of Vermont, Burlington, VT 05405, USA

[2] - Department of Microbiology and Immunology, University of Michigan School of Medicine, Ann Arbor, MI 48109, USA

[*] – corresponding author: bruno.mdigenova@med.uvm.edu

**Abstract**

*Toxoplasma gondii* cannot synthesize purines de novo and must import them; yet, the functional interplay among its four equilibrative nucleoside transporters (ENTs) homologs remains unclear. We systematically deconstructed this network by combining CRISPR-Cas9 knockouts with an auxin-inducible degron. Across all phenotypic assays, tachyzoite replication, nucleoside-analogue sensitivity, alkaline-stress–induced differentiation, and murine cyst formation, the Δ*TgENT2* strain was indistinguishable from the parental line, indicating that TgENT2 is dispensable under the conditions tested. In contrast, the double mutant Δ*TgAT1ΔTgENT3* exhibited delayed bradyzoite differentiation in vitro and produced smaller brain cysts in vivo. This double deletion triggered a ~3-fold transcriptional up-regulation of *TgENT1*, whose product we partially localized to the plant-like vacuolar compartment (PLVAC). Conditional depletion of

TgENT1 caused complete intracellular growth arrest, PLVAC swelling, and a purine-starvation-like transcriptomic program enriched for nucleoside phosphatases and cyclic-nucleotide phosphodiesterases. These findings reveal a compensatory salvage pathway in which the parasite reroutes purine acquisition through a vacuolar route when plasma-membrane import is compromised. Although this adaptation sustains tachyzoite proliferation, it fails during the energetically demanding transition to bradyzoites, creating a metabolic bottleneck that impairs chronic infection. Our work reveals an adaptable yet ultimately limited purine-import network and identifies TgENT1, along with the vacuolar salvage axis it mediates, as a promising therapeutic target for blocking lifelong toxoplasmosis.

## Introduction

*Toxoplasma gondii* is an obligate intracellular parasite that causes toxoplasmosis, a disease affecting approximately one-third of the global population and posing risks to immunocompromised individuals and developing fetuses. The parasite's lifecycle includes acute (tachyzoite) and chronic (bradyzoite) stages, each characterized by distinct metabolic demands [1]. A critical adaptation of *T. gondii* is its complete reliance on host-derived purines due to the absence of a *de novo* purine synthesis pathway [2]. Understanding how *T. gondii* transports and manages purine resources is crucial for deciphering its survival strategies and identifying potential therapeutic targets. Equilibrative nucleoside transporters (ENTs) are key proteins involved in this purine acquisition from host cells [3]. Here we investigate the roles of four putative *T. gondii* ENTs: TgENT1 (TGME49_288540), TgENT2 (TGME49_500147), TgENT3 (TGME49_233130), and TgAT1 (TGME49_244440) across both acute and chronic stages, aiming to elucidate their distinct and overlapping functions in parasite survival and development.

*De novo* nucleic acid synthesis and salvage pathways are fundamental for cellular growth and survival, allowing cells to adapt to varying environmental conditions [4]. Higher eukaryotes possess sophisticated mechanisms to modulate nucleoside transport, salvage, and metabolism, integrating intracellular and extracellular cues to maintain nucleotide homeostasis [5–9].

Many early branching eukaryotes have evolved complex mechanisms to adapt to fluctuating nucleoside availability [10–12]. *T. gondii* exemplifies this adaptation through its complete dependence on host-derived purines, having lost the capacity for *de novo*

purine synthesis during evolution [2,11,13]. This reliance underscores the importance of understanding the mechanisms of purine acquisition in *T. gondii*. In host cells such as macrophages and neurons, purine levels are tightly regulated, presenting a challenging environment for the parasite [9,14].

The parasite employs equilibrative nucleoside transporters (TgENTs) as its primary means of scavenging purines from the host [15]. *T. gondii* utilizes two purine salvage pathways: the phosphorylation of adenosine by the enzyme adenosine kinase and the phosphoribosylation of purine nucleobases by hypoxanthine-guanine phosphoribosyltransferase (HXGPRT) [11]. These pathways enable the parasite to salvage both adenosine and other purine nucleobases efficiently. Additionally, *T. gondii* possesses a functional *de novo* pyrimidine biosynthesis pathway, with uracil phosphoribosyltransferase (UPRT) facilitating pyrimidine salvage by converting uracil to uridine monophosphate [11].

The initial identification of equilibrative nucleoside transporter (ENT) activity in *T. gondii* was demonstrated in extracellular tachyzoites, where adenosine, inosine, and hypoxanthine were transported into the parasite [16]. Subsequent studies identified TgAT1 via insertional mutagenesis[17]. Radioactive nucleoside incorporation assays revealed the presence of multiple nucleoside transporters in *T. gondii*, suggesting a complex system with at least one high-affinity adenosine transporter yet to be characterized [18]. TgAT1 remains the only TgENT studied *in vitro* using heterologous expression systems [15].

In this study, we aim to elucidate the roles of TgAT1 and three other homologs, TgENT1, TgENT2, and TgENT3, across different developmental stages of *T. gondii*. We hypothesized that the network of purine transporters in *T. gondii* is characterized by

functional redundancy and compensatory regulation, ensuring parasite survival under purine stress. To test this, we employed a systematic genetic approach to deconstruct this network by the investigation of the parasite's adaptive response to each TgENT disruption; and assess the importance of this transporter network for the critical developmental transition from the acute tachyzoite to the chronic bradyzoite stage. This strategy was designed to unmask the latent functions and regulatory connections within the purine acquisition machinery.

## Results:

**TgENT BLAST Analysis:** We performed protein-protein BLAST or position-specific iterated BLAST on NCBI using Human ENT-1[3] and *Plasmodium falciparum* PfENT1[12] nucleoside transporters as query sequences to search for *T. gondii* sequences with high similarity. Phylogenetic analysis (**Fig. 1A**) places TgAT1 and TgENT1–3 in a single, well-supported clade with apicomplexan and mammalian ENTs. Conserved-domain searches and AlphaFold modelling suggest that TgAT1 and TgENT1-3 harbor the hallmark 11- ENT fold with an open central pore (**Fig. 1B,C**, and **Table 1**). Pairwise structural comparisons to the HsENT1 crystal structure (PDB 6OB7) show pore dimensions within the expected range for functional ENT homologues (**Fig. 1C**), supporting their candidacy as bona fide transporters. Finally, re-analysis of the transcriptomic data[19,20] (**Fig. 1D**) reveals distinct but overlapping expression patterns; TgAT1 and TgENT1 are abundant throughout enteric, tachyzoite, and bradyzoite stages, TgENT3 is moderately expressed across the life cycle, and TgENT2 peaks during sporulation, suggesting stage-specific expression. A multiple-sequence

alignment of TgENT1, TgENT2, TgENT3, TgAT1, and other characterized ENT homologs from different organisms is provided in Supplementary **Figures S1**.

**Nucleoside analogs growth assay:** We hypothesized that the deletion of genes encoding nucleoside transporter homologs would negatively affect parasite growth. However, none of the single knockout strains displayed significant differences in either short-term or long-term growth rates compared to the parental strain (**Fig. S2**). The growth phenotype of TgENT1 knockdown parasites is described separately below (**Fig. 4**).

Among the four ENT homologs in *Toxoplasma gondii*, only TgAT1 has been biochemically characterized[15]. To determine whether deletion of TgENT2, TgENT3, or TgAT1 alters parasite sensitivity to the toxic nucleoside analogs 9-β-D-arabinofuranosyladenine (Ara-A)[18] and 5-fluorouracil (5-FU)[21], we grew the respective knockout strains in 96-well plates for three days in the presence of increasing concentrations of each analog. Infected monolayers were then fixed and stained with a rabbit anti-*Toxoplasma* (anti-Tg) antibody. Using immunofluorescence microscopy, we measured the area of at least 50 parasitophorous vacuoles (PVs) per condition; the mean PV size served as a quantitative read-out of growth inhibition (**Fig. 2**).

Consistent with TgAT1's role as a purine transporter[15], ΔTgAT1 parasites showed increased resistance to the adenosine analog Ara-A (**Fig. 2A**). Unexpectedly, ΔTgAT1 also exhibited resistance to the pyrimidine analog 5-FU (**Fig. 2B**), suggesting broader substrate specificity than previously recognized. In contrast, the ΔTgENT2 strain did not differ from the parental line (**Fig. 2**), likely because TgENT2 is not expressed during the

tachyzoite stage (**Fig. 1D**). Similarly, the ΔTgENT3 single knockout showed no difference in sensitivity relative to the parental line under drug treatment (**Fig. 2**). However, the double knockout ΔTgAT1ΔTgENT3 formed significantly larger PVs than ΔTgAT1 under 10 μM Ara-A, indicating that deletion of TgENT3 further enhances resistance to this analog. Conversely, ΔTgAT1ΔTgENT3 vacuoles were significantly smaller than those of ΔTgAT1 under 5 μM 5-FU, although they remained larger than parental vacuoles. Collectively, these observations suggest that while TgENT3 deletion may confer increased resistance to Ara-A in the ΔTgAT1ΔTgENT3 background, it also leads to heightened sensitivity to 5-FU.

**Role of TgENTs homologs in chronic infection:** We successfully generated knockout strains for TgAT1, TgENT2, and TgENT3 using CRISPR/Cas9-mediated gene disruption in the ME49 background. Multiple attempts to generate a TgENT1 knockout strain were unsuccessful, suggesting this gene may be essential for parasite viability. This prompted us to instead use the mini auxin-inducible degron (mAID) system for conditional knockdown analysis (**Fig. 4**) in the RH background.

Based on published transcriptomic data[19,20] (**Fig. 1D**), TgENT1, TgENT3, and TgAT1 are constitutively expressed throughout the parasite life cycle, whereas TgENT2 expression is restricted to bradyzoite and sexual developmental stages, explaining the lack of phenotype in tachyzoite growth assays. Given this distinct expression pattern, as well as the unexpected lack of growth defects in single knockout strains, we next investigated potential changes in cyst formation using an *in vitro* and *in vivo* model.

We assessed the impact of TgENT deletion on parasite differentiation by culturing human foreskin fibroblasts (HS27) infected monolayers cultured in RPMI medium adjusted to pH 8.2 and atmospheric $CO_2$. Monolayers were fixed after two, three, or seven days, and differentiation rates were quantified using immunofluorescence assays (IFA) with the lectin Dolichos Biflorus Agglutinin (DBA), which stains *T. gondii's* cyst wall[22]. Parasites were co-stained with anti-Tg antibody, which identifies both tachyzoites and bradyzoites, to quantify all vacuoles in the monolayers and calculate differentiation ratios among strains. ΔTgAT1 and ΔTgAT1ΔTgENT3 parasites exhibited significantly slower differentiation. Both ΔTgAT1 and ΔTgAT1ΔTgENT3 have delayed differentiation, exemplified by lower number of DBA vacuoles in the population (**Fig. 3A**). Moreover, after 3 days in pH 8.2 medium, the DBA-positive vacuoles formed by ΔTgAT1 and ΔTgAT1ΔTgENT3 parasites are smaller than parental and complement strains (**Fig. S3**). By day 7, only 88% of ΔTgAT1 and 63% of ΔTgAT1ΔTgENT3 parasites were DBA-positive, compared to approximately 99% in the parental and ΔTgENT3 strains (**Fig. 3A**). As we noticed at day 3, the ΔTgAT1 and ΔTgAT1ΔTgENT3 DBA positive vacuoles are significantly smaller at day 7 as well compared to other strains (**Fig. 3B**). While ΔTgENT3 did not show a reduction in differentiation rate, the accentuated phenotype in the double deleted strain suggests an interplay between TgAT1 and TgENT3 in parasite differentiation under alkaline stress.

To assess long-term differentiation *in vivo*, male C57BL/6 mice were intraperitoneally infected with 250 parasites. Four weeks post-infection, mice were euthanized in accordance with Institutional Animal Care and Use Committee (IACUC) guidelines. Brains were extracted surgically, homogenized in PBS through sequential passage

using 18-, 20-, and 22-gauge needles, fixed, and stained with DBA. Cyst numbers and sizes were quantified for each strain, as previously done[23], (**Fig. S4**). This experiment was independently replicated twice, with four mice per strain in each replicate. No significant differences in cyst counts were observed among the strains (**Fig. S4A**). These findings suggest that, despite initially impaired differentiation observed in ΔTgAT1 and ΔTgAT1ΔTgENT3 parasites, these mutants ultimately compensate for this deficit during chronic infection in mice. The cyst sizes for ΔTgENT3 and ΔTgAT1ΔTgENT3 were significantly lower compared to all other strains, suggesting that TgENT3 may have important roles during bradyzoite replication, as cyst sizes are proportional to parasite growth (**Fig. S4B**).

To investigate whether the comparable tachyzoite growth rate (**Fig. S2**) observed in ΔTgAT1ΔTgENT3 was due to compensatory expression of another TgENT family member, we performed quantitative PCR (qPCR) analyses. We compared the expression levels of the remaining TgENT transporters, TgENT1 and TgENT2, across tachyzoites derived from ΔTgAT1ΔTgENT3, single knockout strains, and the parental strain. qPCR analysis revealed a ~3-fold upregulation of TgENT1 transcripts specifically in ΔTgAT1ΔTgENT3 parasites compared to parental controls ($p < 0.05$), while TgENT2 expression remained unchanged (**Fig. 4A**). Notably, single knockout strains, ΔTgAT1 and ΔTgENT3, showed no compensatory changes in TgENT1 or TgENT2 (**Fig. 4A**). These data indicate that the absence of both TgAT1 and TgENT3 may trigger compensatory upregulation of TgENT1, maintaining tachyzoite growth rates similar to single knockout strains.

**TgENT1 conditional deletion results in complete growth arrest:** TgENT1 has a markedly negative genome-wide CRISPR phenotype score of –3.68[24]. On this scale, increasingly negative values typically denote progressively stronger fitness costs, underscoring TgENT1's critical importance for parasite survival (**Table 1**). To investigate the role of TgENT1, we developed a parasite line, TgENT1-mAID-HA, in RH backgrond with regulated TgENT1 expression via 3-indoleacetic acid (IAA) treatment [25]. We assessed the impact of TgENT1 depletion on parasite growth by culturing the parasites with IAA for 48 hours. The treated parasites exhibited reduced replication when invading new HS27 monolayers (**Fig. 4B and C**), indicating that TgENT1 expression is crucial for normal growth and replication. Additionally, a long-term growth defect was observed over nine days of continuous culture, as evidenced by the formation of smaller and fewer plaques (**Fig. 4D**).

**TgENT1 partially colocalizes to the PLVAC:** Using the TgENT1-mAID-HA construct, we were able to visualize the association of TgENT1 within *T. gondii* parasites. When cultured with 500 µM indole-3-acetic acid (IAA), we observed the disappearance of the TgENT1 signal, confirming the system functionality (**Fig. 5**). Surprisingly, TgENT1 localization differed markedly from typical plasma membrane-associated ENTs. Instead, HA-TgENT1 displayed a distinctive punctate pattern within the parasite cytoplasm, suggesting it is localized within intracellular organelles (**Fig. 5**).

To pinpoint the intracellular compartment that hosts TgENT1, we performed immunofluorescence assays (IFA) on parasites expressing HA-tagged TgENT1 alongside well-validated organelle markers. Co-staining was carried out with antibodies

against cathepsin protease L (TgCPL) and the chloroquine-resistance transporter (TgCRT), both definitive markers of the plant-like vacuole (PLVAC)[26], as well as the propeptide of microneme protein 2 (TgProM2AP), which labels the endosome-like compartment [27], and an anti-apicoplast (TgAtrx1) antibody[28]. Here, M(X) represents Manders' colocalization coefficients which quantify the fraction of antibody X's fluorescence that shares the same pixels as the HA signal (1.0 = complete overlap; 0 = none). Across all markers, in control conditions, the TgENT1 HA-tagged protein shows partial colocalization with PLVAC markers: TgCPL (Pearson's r =0.84; M(CPL) =0.90) and TgCRT (Pearson's r =0.79; M(CRT) =0.54), weak overlap by the microneme protein TgProM2AP (Pearson's r =0.61; M(M2AP) =0.09), and virtually no overlap with TgAtrx1(Pearson's r =0.10; M(Atrx1) =0.05). After IAA-induced depletion, Manders' coefficients collapse to near background (TgCPL 0.08; TgCRT 0.02; TgProM2AP 0.09; TgAtrx1 0.00) and Pearson's r values likewise fall (CPL 0.21; CRT 0.03; ProM2AP 0.25; Atrx1 0.05), indicating loss of specific HA signal and that the residual fluorescence no longer maps to these organelles. Manders and Pearson's colocalization coefficients are based on three different biological experiments. Together, these results identify the PLVAC as the principal compartment for TgENT1.

**PLVAC measurement:** Given the partial colocalization of TgENT1 and TgCRT and TgCPL (**Fig. 5**), we evaluated PLVAC morphology following TgENT1 depletion by performing knockdown experiments in replicating parasites 36 hours post-infection. Parasites were mechanically liberated and subsequently inoculated onto fresh HS27 monolayers for 30 minutes before fixation and staining. Importantly, TgENT1

knockdown parasites retained their ability to invade host cells efficiently. Immunofluorescence assays were employed to measure PLVAC dimensions using an anti-TgCPL antibody (**Fig. 6**). Area from 50 TgCPL puncta per experimental condition were measured in triplicate, and comparative statistical analyses were performed using t-test. Consistent with our hypothesis, TgENT1 depletion resulted in measurable swelling of the PLVAC, further implicating TgENT1 as important for maintaining PLVAC homeostasis.

**Transcriptomic analysis of TgENT1 knockdown:** Transcriptomic profiling following conditional knockdown of TgENT1 revealed significant alterations in genes associated with purine metabolism, reinforcing TgENT1's proposed function as a nucleoside transporter (**Fig. 7**). Principal-component analysis (**Fig. 7A**) cleanly separates IAA-treated and control tachyzoites along PC1 and shows a further time-dependent shift on PC2, underscoring a rapid and progressive transcriptional response to TgENT1 loss. An accompanying heat-map of (**Fig. 7B**) highlights the 50 most variable transcripts. Volcano plots of differentially expressed genes (**Fig. 7C**) display a broader and more pronounced response by 48 h, with the number and magnitude of regulated transcript expanding and purine-stress markers (e.g., nucleoside phosphatases and phosphodiesterases) among the most strongly up-regulated. For example, TGGT1_225290 (GDA1/CD39 nucleoside phosphatase) demonstrated progressive upregulation from day 1 ($\log_2$ fold change = 2.98) to day 2 ($\log_2$ fold change = 6.21). Similarly, TGGT1_259960 (putative nucleoside-diphosphatase) exhibited strong induction from day 1 ($\log_2$ fold change = 2.81) to day 2 ($\log_2$ fold change = 5.92),

suggesting a sustained compensatory effort to restore purine homeostasis when nucleoside uptake is impaired. Importantly, other TgENT family members showed no significant expression changes.

In total, 208 transcripts were already altered at 24 h and this number more than doubled by 48 h, with 96 up- and 58 down-regulated genes shared between both time points (**Fig. 7D**), defining a core TgENT1-dependent regulon. Among the induced genes were several 3'5'-cyclic nucleotide phosphodiesterases (PDEs), notably PDE3 (TGGT1_233065; $\log_2$ fold change = 1.30 at day 1, significantly increased to 3.88 at day 2), and PDE17 (TGGT1_257945; $\log_2$ fold change = 2.92), suggesting heightened cyclic nucleotide turnover and signaling adaptation [29].

KEGG pathway analyses (**Fig. 6E**) revealed significant differential expression in pathways related to purine metabolism, nitrogen compound metabolism, and oxidoreductase activities. The enrichment of the purine metabolism pathway further intensified at day 2, according to KEGG pathway analysis (**Fig. 7E**) (fold enrichment = 2.39, p-value = 0.0008), featuring upregulated genes like TGGT1_230555[30] (adenylate/guanylate cyclase; $\log_2$ fold change = 3.84) and further emphasizing signaling changes upon TgENT1 knockdown. Additionally, TGGT1_290970[31] (8-amino-7-oxononanoate synthase), involved in biotin biosynthesis, was substantially induced from day 1 ($\log_2$ fold change = 2.57) to day 2 ($\log_2$ fold change = 5.22), suggesting enhanced biotin-dependent metabolic processes.

Collectively, these transcriptomic findings suggest TgENT1's central role in purine transport and homeostasis within *T. gondii*. The extensive and progressive compensatory responses triggered by TgENT1 knockdown, including purine salvage,

metabolic reprogramming, and signaling adaptations, provide new insights into the parasite's ability to adapt to disrupted nucleoside transport.

## Discussion

In this study, we have expanded the model of purine acquisition in *Toxoplasma gondii*, moving beyond a simple linear import pathway to reveal a dynamic, regulated network. HyperLOPIT spatial-proteomics has previously assigned both TgAT1 and TgENT3 to the parasite plasma membrane[36] **(Table 1)**. Although our experiments did not verify this localization directly, the functional data reveal a broader principle of *metabolic resilience*: *Toxoplasma gondii* can rapidly re-wire its purine-uptake network to compensate for the loss of TgAT1 and TgENT3. Such plasticity is indispensable for an organism that is purine-auxotrophic and therefore wholly dependent on the host for nucleoside acquisition [32]. Importantly, we also demonstrate that this adaptive capacity is limited during differentiation (**Fig. 3**). Understanding the mechanics, function, and ultimate failure point of this network provides unprecedented insight into the metabolic strategies governing the parasite's lifecycle.

Our data show that deletion of the TgAT1 and TgENT3 triggers specific transcriptional upregulation of TgENT1 (**Fig. 4A**), a transporter that our localization studies showed to partially localize in the Plant-Like Vacuolar Compartment (PLVAC) (**Fig. 5**). These findings support a model where the parasite mobilizes an alternative salvage pathway. This pathway might rely on acquiring purines from the degradation of host-derived nucleic acids within the acidic, digestive environment of the PLVAC[26] or from the recycling of its own nucleic acids, a function consistent with the PLVAC's role in

trafficking and catabolism [26]. The adaptive function of the PLVAC and TgENT1 creates a crucial lifeline that sustains a baseline of purine homeostasis.

While this adaptive axis provides metabolic flexibility for tachyzoites, its capacity is finite, and its functional limit is most profoundly revealed during the critical developmental transition to the chronic stage. The failure of the ΔTgAT1ΔTgENT3 strain to develop as bradyzoites *in vitro* (**Fig. 3A and C,** and **S3**) likely stems from two interconnected deficiencies: a substrate and a signaling deficit. The substrate deficit may deplete critical precursors for cyst formation, including the sugar-nucleotide donors uridine diphosphate N-acetyl-D-glucosamine (UDP-GlcNAc) and uridine diphosphate N-acetyl-D-galactosamine (UDP-GalNAc). These activated sugars supply N-acetylglucosamine and N-acetylgalactosamine residues that decorate cyst-wall glycoconjugates and are important for proper wall assembly [33]. More critically, however, this purine starvation likely precipitates a failure in cellular signaling. Purine salvage is the sole source of the adenosine required for ATP synthesis. ATP, in turn, is the exclusive substrate for adenylyl cyclases that generate cyclic AMP (cAMP), a master second messenger in *T. gondii*. The cAMP signaling pathway is known to be an important regulator of stage conversion, with fluctuations in cAMP levels acting as a key signal for maintaining the tachyzoite state or initiating differentiation into bradyzoites [34]. Therefore, we propose that the ΔTgAT1ΔTgENT3 strain, while receiving the external cues to differentiate (e.g., alkaline stress), is metabolically incapable of mounting the appropriate cAMP signaling response required to execute this complex developmental program. Interestingly, although ΔTgAT1ΔTgENT3 mutants form smaller cysts than parental strains in mice, the total cyst burden remains unchanged, suggesting that the

30-day *in vivo* period allows the parasites to overcome the differentiation delay observed *in vitro* (**Fig. S4**).

Our study illuminates a clear transcriptional and phenotypic signature of nucleoside starvation in the absence of TgENT1, and several open questions make the next experimental steps especially compelling. First, the robust up-regulation of TgENT1 is currently inferred to reflect enhanced host-nucleoside scavenging; confirming this hypothesis with direct radiolabeled-substrate uptake assays will test our model and establish quantitative benchmarks for future transporter engineering. Second, the nucleoside-depletion phenotype reported for Δgra14 parasites, which are defective in parasite endocytosis of material from the cytosol of infected cells, suggests that the PLVAC has a central role in nucleoside salvage and invites a systematic dissection of each vacuolar effector in that pathway [35]. Finally, untargeted metabolomics coupled to parallel measurements of high-energy substrates such as ATP and GTP and their signaling derivatives would provide a systems-level view of how disrupted uptake reverberates through the parasite's metabolic and regulatory networks.

Ultimately, by deconstructing this purine acquisition network, we have revealed a dynamic interplay between metabolic adaptation and developmental signaling. The biological consequence of this network's failure is unambiguous. By uncovering a scenario where the parasite's adaptive capacity breaks down at the nexus of metabolism and developmental signaling, we have exposed a significant vulnerability. This metabolic bottleneck, where purine insufficiency hypothetically precipitates a signaling failure that blocks the establishment of chronic infection, represents a highly promising and conceptually novel target for therapeutic intervention. Further

investigation offers the potential to develop strategies aimed specifically at disrupting the lifelong persistence that is the clinical hallmark of toxoplasmosis.

**References:**


1. Dubey JP, Jones JL. Toxoplasma gondii infection in humans and animals in the United States. Int J Parasitol. England; 2008 Sept;38(11):1257–1278. PMID: 18508057

2. Krishnan A, Kloehn J, Lunghi M, Chiappino-Pepe A, Waldman BS, Nicolas D, Varesio E, Hehl A, Lourido S, Hatzimanikatis V, Soldati-Favre D. Functional and Computational Genomics Reveal Unprecedented Flexibility in Stage-Specific Toxoplasma Metabolism. Cell Host Microbe. United States; 2020 Feb 12;27(2):290-306.e11. PMID: 31991093

3. Wright NJ, Lee SY. Structures of human ENT1 in complex with adenosine reuptake inhibitors. Nature Structural & Molecular Biology. 2019 July 1;26(7):599–606.

4. Pareek V, Pedley AM, Benkovic SJ. Human de novo purine biosynthesis. Crit Rev Biochem Mol Biol. 2021 Feb;56(1):1–16. PMCID: PMC7869020

5. Verrier F, An S, Ferrie AM, Sun H, Kyoung M, Deng H, Fang Y, Benkovic SJ. GPCRs regulate the assembly of a multienzyme complex for purine biosynthesis. Nat Chem Biol. 2011 Oct 23;7(12):909–915. PMID: 22020552

6. Huang Z, Xie N, Illes P, Di Virgilio F, Ulrich H, Semyanov A, Verkhratsky A, Sperlagh B, Yu SG, Huang C, Tang Y. From purines to purinergic signalling: molecular functions and human diseases. Signal Transduct Target Ther. 2021 Apr 28;6(1):162. PMID: 33907179

7. Mason S. Signaling for purines. Nature Structural & Molecular Biology. 2011 Dec 1;18(12):1322–1322.

8. Jain S, Jacobson KA. Purinergic signaling in diabetes and metabolism. Biochem Pharmacol. 2021 May;187:114393. PMID: 33359363

9. Soler C, García-Manteiga J, Valdés R, Xaus J, Comalada M, Casado FJ, Pastor-Anglada M, Celada A, Felipe A. Macrophages require different nucleoside transport systems for proliferation and activation.

10. Carter NS, Yates PA, Gessford SK, Galagan SR, Landfear SM, Ullman B. Adaptive responses to purine starvation in Leishmania donovani. Mol Microbiol. 2010 Oct;78(1):92–107. PMCID: PMC2964060

11. Fox BA, Bzik DJ. Biochemistry and metabolism of Toxoplasma gondii: purine and pyrimidine acquisition in Toxoplasma gondii and other Apicomplexa. 2020 Jan 1;397–449.

12. Wang C, Yu L, Zhang J, Zhou Y, Sun B, Xiao Q, Zhang M, Liu H, Li J, Li J, Luo Y, Xu J, Lian Z, Lin J, Wang X, Zhang P, Guo L, Ren R, Deng D. Structural basis of the substrate recognition and inhibition mechanism of Plasmodium falciparum

nucleoside transporter PfENT1. Nat Commun. England; 2023 Mar 28;14(1):1727. PMCID: PMC10050424

13. Kloehn J, Hammoudi PM, Soldati-Favre D. Metabolite salvage and restriction during infection — a tug of war between Toxoplasma gondii and its host. Current Opinion in Biotechnology. 2021 Apr 1;68:104–114. PMID: 33202353

14. Dunwiddie TV, Masino SA. The Role and Regulation of Adenosine in the Central Nervous System. Annu Rev Neurosci. Annual Reviews; 2001 Mar 1;24(1):31–55.

15. Campagnaro GD, Elati HAA, Balaska S, Martin Abril ME, Natto MJ, Hulpia F, Lee K, Sheiner L, Van Calenbergh S, de Koning HP. A Toxoplasma gondii Oxopurine Transporter Binds Nucleobases and Nucleosides Using Different Binding Modes. International Journal of Molecular Sciences. 2022 Jan;23(2):710. PMID: 35054895

16. Conrad Schwab J, Afifi Afifi M, Pizzorno G, Handschumacher RE, Joiner KA. Toxoplasma gondii tachyzoites possess an unusual plasma membrane adenosine transporter. Molecular and Biochemical Parasitology. 1995 Mar 1;70(1):59–69. PMID: 7637715

17. Chiang CW, Carter N, Sullivan WJ, Donald RGK, Roos DS, Naguib FNM, Kouni MH el, Ullman B, Wilson CM. The Adenosine Transporter of Toxoplasma gondii: IDENTIFICATION BY INSERTIONAL MUTAGENESIS, CLONING, AND RECOMBINANT EXPRESSION *. Journal of Biological Chemistry. Elsevier; 1999 Dec 3;274(49):35255–35261. PMID: 10575012

18. De Koning HP, Al-Salabi MI, Cohen AM, Coombs GH, Wastling JM. Identification and characterisation of high affinity nucleoside and nucleobase transporters in Toxoplasma gondii. International Journal for Parasitology. 2003 July 30;33(8):821–831.

19. Hehl AB, Basso WU, Lippuner C, Ramakrishnan C, Okoniewski M, Walker RA, Grigg ME, Smith NC, Deplazes P. Asexual expansion of Toxoplasma gondii merozoites is distinct from tachyzoites and entails expression of non-overlapping gene families to attach, invade, and replicate within feline enterocytes. BMC Genomics. England; 2015 Feb 13;16(1):66. PMCID: PMC4340605

20. Ramakrishnan C, Maier S, Walker RA, Rehrauer H, Joekel DE, Winiger RR, Basso WU, Grigg ME, Hehl AB, Deplazes P, Smith NC. An experimental genetically attenuated live vaccine to prevent transmission of Toxoplasma gondii by cats. Sci Rep. England; 2019 Feb 6;9(1):1474. PMCID: PMC6365665

21. Elati HAA, Goerner AL, Martorelli Di Genova B, Sheiner L, de Koning HP. Pyrimidine salvage in Toxoplasma gondii as a target for new treatment. Front Cell Infect Microbiol. 2023;13:1320160. PMCID: PMC10755004

22. Zhang YW, Halonen SK, Ma YF, Wittner M, Weiss LM. Initial characterization of CST1, a Toxoplasma gondii cyst wall glycoprotein. Infect Immun. United States; 2001 Jan;69(1):501–507. PMCID: PMC97909

23. Watts E, Zhao Y, Dhara A, Eller B, Patwardhan A, Sinai AP. Novel Approaches Reveal that Toxoplasma gondii Bradyzoites within Tissue Cysts Are Dynamic and Replicating Entities In Vivo. mBio. United States; 2015 Sept 8;6(5):e01155-01115. PMCID: PMC4600105

24. Sidik SM, Huet D, Ganesan SM, Huynh MH, Wang T, Nasamu AS, Thiru P, Saeij JPJ, Carruthers VB, Niles JC, Lourido S. A Genome-wide CRISPR Screen in Toxoplasma Identifies Essential Apicomplexan Genes. Cell. 2016 Sept 8;166(6):1423-1435.e12. PMID: 27594426

25. Brown KM, Long S, Sibley LD. Conditional Knockdown of Proteins Using Auxin-inducible Degron (AID) Fusions in Toxoplasma gondii. Bio Protoc. 2018 Feb 20;8(4):e2728. PMCID: PMC5890294

26. Stasic AJ, Moreno SNJ, Carruthers VB, Dou Z. The Toxoplasma plant-like vacuolar compartment (PLVAC). J Eukaryot Microbiol. United States; 2022 Nov;69(6):e12951. PMCID: PMC10576567

27. Gaji RY, Flammer HP, Carruthers VB. Forward targeting of Toxoplasma gondii proproteins to the micronemes involves conserved aliphatic amino acids. Traffic. England; 2011 July;12(7):840–853. PMCID: PMC3115430

28. DeRocher AE, Coppens I, Karnataki A, Gilbert LA, Rome ME, Feagin JE, Bradley PJ, Parsons M. A thioredoxin family protein of the apicoplast periphery identifies abundant candidate transport vesicles in Toxoplasma gondii. Eukaryot Cell. United States; 2008 Sept;7(9):1518–1529. PMCID: PMC2547066

29. Moss WJ, Patterson CE, Jochmans AK, Brown KM. Functional Analysis of the Expanded Phosphodiesterase Gene Family in Toxoplasma gondii Tachyzoites. mSphere. United States; 2022 Feb 23;7(1):e0079321. PMCID: PMC8809380

30. Brown KM, Sibley LD. Essential cGMP Signaling in Toxoplasma Is Initiated by a Hybrid P-Type ATPase-Guanylate Cyclase. Cell Host Microbe. United States; 2018 Dec 12;24(6):804-816.e6. PMCID: PMC6292738

31. Asady B, Dick CF, Ehrenman K, Sahu T, Romano JD, Coppens I. A single Na+-Pi cotransporter in Toxoplasma plays key roles in phosphate import and control of parasite osmoregulation. PLoS Pathog. United States; 2020 Dec;16(12):e1009067. PMCID: PMC7817038

32. Schwartzman JD, Pfefferkorn ER. Toxoplasma gondii: Purine synthesis and salvage in mutant host cells and parasites. Experimental Parasitology. 1982 Feb 1;53(1):77–86.

33. Caffaro CE, Koshy AA, Liu L, Zeiner GM, Hirschberg CB, Boothroyd JC. A nucleotide sugar transporter involved in glycosylation of the Toxoplasma tissue cyst wall is required for efficient persistence of bradyzoites. PLoS Pathog. United States; 2013;9(5):e1003331. PMCID: PMC3642066

34. Sugi T, Ma YF, Tomita T, Murakoshi F, Eaton MS, Yakubu R, Han B, Tu V, Kato K, Kawazu SI, Gupta N, Suvorova ES, White MW, Kim K, Weiss LM. Toxoplasma gondii Cyclic AMP-Dependent Protein Kinase Subunit 3 Is Involved in the Switch from Tachyzoite to Bradyzoite Development. mBio. American Society for Microbiology; 2016 May 31;7(3):10.1128/mbio.00755-16.

35. Rimple PA, Olafsson EB, Markus BM, Wang F, Augusto L, Lourido S, Carruthers VB. Metabolic adaptability and nutrient scavenging in Toxoplasma gondii: insights from ingestion pathway-deficient mutants. mSphere. United States; 2025 Apr 29;10(4):e0101124. PMCID: PMC12039266

36. Barylyuk K, Koreny L, Ke H, Butterworth S, Crook OM, Lassadi I, Gupta V, Tromer E, Mourier T, Stevens TJ, Breckels LM, Pain A, Lilley KS, Waller RF. A Comprehensive Subcellular Atlas of the Toxoplasma Proteome via hyperLOPIT Provides Spatial Context for Protein Functions. Cell Host & Microbe. 2020 Nov 11;28(5):752-766.e9.

37. Tobin Magle C, Pittman KJ, Moser LA, Boldon KM, Knoll LJ. A toxoplasma patatin-like protein changes localization and alters the cytokine response during toxoplasmic encephalitis. Infect Immun. United States; 2014 Feb;82(2):618–625. PMCID: PMC3911373

## Figure Legends

**Table 1 – BLAST results for *T. gondii* sequences with high similarity with Human ENT1 and *Plasmodium falciparum* ENT1.**

| Gene ID | Name | Localization by hyperLOPIT[36] | PFam ID | PFam Description | Phenotype Score[24] |
|---|---|---|---|---|---|
| **TGME49_233130** | TgENT3 | PM integral, Golgi | PF01733 | Equilibrative nucleoside transporter | 0.04 |
| **TGME49_244440** | TgAT1 | PM integral, Golgi | PF01733 | Equilibrative nucleoside transporter | 1.02 |
| **TGME49_288540** | TgENT1 | None | PF01733 | Equilibrative nucleoside transporter | -3.68 |
| **TGME49_500147** | TgENT2 | None | PF01733 | Equilibrative nucleoside transporter | 0.47 |

**Figure 1 – Figure 1. Evolutionary, structural, and transcriptional overview of the *Toxoplasma gondii* equilibrative nucleoside transporter (TgENT) family.**

**(A)** Phylogenetic relationships: Full-length protein sequences of the four *T. gondii* ENTs (TgAT1, TgENT1–3) were aligned with representative ENT homologs from apicomplexan, fungal, plant, trypanosomatid, and mammalian lineages (CpAT, *Cryptosporidium parvum*; PfENT1, *Plasmodium falciparum*; ScFUN26, *Saccharomyces cerevisiae*; AtENT1, *Arabidopsis thaliana*; NNT, *Naegleria* sp.; LmNnt1-1, *Leishmania major*; HsENT1/2, MmENT1, human and mouse ENT1/2; HsCNT1/2, human concentrative nucleoside transporters—used as the out-group). MUSCLE-aligned sequences were subjected to neighbor-joining analysis; node labels give bootstrap

support from 1,000 replicates (values < 30% omitted). Scale bar, 0.5 substitutions per site.

**(B)** Predicted tertiary structures: AlphaFold models of the four TgENT paralogues are shown in ribbon representation (top-view, upper row; side-view, lower row). Each adopts the canonical 11–13 trans-membrane helix bundle typical of ENT family members, with the central permeation pore clearly visible in the side view. Colors match the gene names in panel A.

**(C)** Quantitative structural comparison to human ENT1 (PDB 6OB7). Pore dimensions were measured along the long and short axes (Å) for each TgENT model and for HsENT1, and Cα-root-mean-square deviations (RMSDs) were calculated after SuperPose alignment to 6OB7. Heat-map shading reflects magnitude (scale bar, right). Cartoon underneath illustrates the pore-width measurements on the HsENT1 template.

**(D)** Stage-specific expression of TgENT transcripts. Heat-map of log2-transformed TPM values (+1) extracted from the ToxoDB developmental transcriptome. EES 1–5, enteroepithelial stages in cat epithelium; sporulating oocysts; tachyzoites; tissue cyst bradyzoites; unsporulated oocysts [19,20]. TgAT1 is highest in enteroepithilial and early tachyzoite stages, TgENT1 is broadly expressed, TgENT2 peaks during sporulation, and TgENT3 shows moderate expression throughout.

**Figure 2. Deletion of TgAT1 and TgENT3 alters *Toxoplasma* sensitivity to toxic nucleoside analogs.** Parental ME49 parasites and the indicated mutants were allowed

to replicate for 72 h in HS27 monolayers in the presence of increasing concentrations of **(A)** the adenosine analog 9-β-D-arabinofuranosyl-adenine (Ara-A) or **(B)** the pyrimidine analog 5-fluorouracil (5-FU) Cultures were fixed, stained with anti-*Toxoplasma* (anti-Tg) antibody, and the mean area of ≥50 parasitophorous vacuoles (PVs) per condition was measured by automated image analysis. Growth inhibition (% ± SEM) was calculated relative to drug-free controls and fitted to a four-parameter logistic curve (GraphPad Prism). Data are from three biological replicates; each performed in technical triplicate. Panel layout: For each drug, individual dose–response curves are shown for the parental line, single knockouts (ΔTgENT3, ΔTgENT2, ΔTgAT1), the double knockout (ΔTgAT1ΔTgENT3), and the corresponding epitope-tagged complementation lines (ΔTgENT3::TgENT3-Ty1, ΔTgAT1::TgAT1-myc). The right-most graph in each row overlays all strains for direct comparison (color key, inset).

**Figure 3 – Simultaneous deletion of TgENT3 and TgAT1 delays differentiation. (A)** Percentage of differentiation of the parental line, single knockouts (ΔTgENT3, ΔTgENT2, ΔTgAT1), the double knockout (ΔTgAT1ΔTgENT3), and the corresponding epitope-tagged complementation lines TgENT3-Ty1 (ΔTgENT3::TgENT3-Ty1) and TgAT1-myc (ΔTgAT1::TgAT1-myc) at day 2, 3, and 7 post invasion of HS27 monolayers cultured in alkaline stress conditions (pH 8.1 and atmospheric $CO_2$). Parasites were stained with immunofluorescent antibodies DAPI, anti-Tg, and DBA. Bars show the percentage of DBA positive vacuoles (thresholds set based on parental line intensity) over total vacuoles (anti-Tg). Slides were imaged with BioTEK Cytation 7 and quantified using the Gen5 software (≥100 vacuoles were counted per replicate, n = 3 biological

replicates). Statistical significance was assessed using one-way ANOVA, (****P < 0.0001, ns = non-significant). **(B)** Average sizes of each cyst (DBA positive vacuole) on day 7 post invasion. **(C)** Representative images of vacuoles from each parasite line. Scale bar, 10 µm

**Figure 4. TgENT1 is transcriptionally upregulated in ΔTgAT1ΔTgENT3 parasites and is indispensable for intracellular replication and plaque formation.**

**(A)** qRT-PCR analysis of compensatory TgENT expression. Total RNA from tachyzoites of the indicated mutant lines was analyzed by qRT-PCR with primers specific for **TgENT1** and **TgENT2**. Bars show $2^{\Delta\Delta Ct}$ values (mean ± SEM, n = 3 biological replicates) normalized to the parental line (dotted line = 1). Only the double knockout (ΔTgAT1ΔTgENT3, open bars) exhibits a ~3-fold induction of TgENT1 (one-way ANOVA with ***P < 0.001); TgENT2 is unchanged (ns).

**(B)** Acute intracellular growth after TgENT1 depletion. TgENT1-mAID-HA parasites were pre-treated for 48 h with vehicle or 500 µM indole-3-acetic acid (+IAA) to trigger auxin-inducible degradation, then allowed to invade fresh HS27 monolayers for a further 48 h under the same conditions. Stacked bars depict the distribution of vacuoles containing 1, 2, 4, 8, 16, 32, 64 or >64 parasites (≥50 vacuoles counted per replicate; 3 replicates).

**(C)** Plaque-formation assay. Wells were inoculated with 50 tachyzoites of the indicated strains and cultured for 9 days ± 500 µM IAA before fixation and crystal-violet staining. Representative wells are shown. **(D)** Quantification of plaque area. Individual plaque areas from TgENT1-mAID-HA wells (vehicle vs +IAA) are plotted (median ± inter-

quartile range; n = 15–20 plaques). Student t-test, ****P < 0.0001. **(E)** Quantification of plaque number. Mean ± SEM plaque counts per well from three independent experiments. T-test, ****, P < 0.0001.

**Figure 5. TgENT1 resides in the PLVAC and is eliminated by auxin-induced degradation.** Representative immunofluorescence images of TgENT1-mAID-HA tachyzoites pre-treated for 48 h with vehicle or 500 µM indole-3-acetic acid (+IAA), then grown in fresh HS27 monolayers for a further 48 h under the same conditions. Parasites were fixed and stained with anti-HA (second column) plus one of the indicated compartment markers (third column): *T. gondii* cathepsin protease L (TgCPL) or *T. gondii* chloroquine-resistance transporter (TgCRT) for the PLVAC, TgAtrx1 for the apicoplast, and TgProM2AP for the endosome-like/microneme compartment. Columns show (left to right) phase-contrast, anti-HA, co-stain, DAPI, and the merged overlay (anti-HA = green, co-stain = magenta, DAPI = blue). Under vehicle conditions TgENT1-HA displays a punctate pattern that co-localizes with PLVAC markers TgCPL and TgCRT, but only weakly with TgProM2AP and not with TgAtrx1, consistent with predominant residence in PLVAC. Upon IAA treatment the HA signal is virtually abolished, confirming efficient auxin-inducible degradation. Scale bar, 10 µm.

**Figure 6. Loss of TgENT1 causes swelling of the PLVAC. (A).** TgENT1-mAID-HA parasites were grown for 48 h post-infection, mechanically released, and allowed to reinvade new HS27monolayers for 30 minutes in the continued presence of vehicle or 500 µM IAA. Cells were fixed and co-stained with anti-HA (TgENT1, green) and anti-

TgCPL (PLVAC marker, magenta); nuclei were counter-stained with DAPI (blue). TgENT1 is readily detected in the central PLVAC punctum under vehicle conditions but is efficiently depleted after auxin treatment, coincident with an enlarged TgCPL-positive compartment. Scale bar, 10 µm.

**(B) Quantification of PLVAC size.** Area of 50 individual CPL-positive structures per condition (three independent experiments) was measured in FIJI. Box-and-whisker plots show median, inter-quartile range, and 5th–95th percentiles. Auxin-induced TgENT1 depletion increased PLVAC area nearly five-fold, student t-test, **** $P < 0.0001$, suggesting that TgENT1 activity is required to maintain normal vacuolar homeostasis.

**Figure 7. Transcriptomic response to acute TgENT1 depletion reveals a progressive, purine-centric stress program.** TgENT1-mAID-HA tachyzoites (three biological replicates) were pre-treated for 48 h with vehicle or 500 µM IAA, then allowed to invade fresh HS27 monolayers under the same conditions and harvested 24 h (Day 1) or 48 h (Day 2) after invasion. Poly-(A) RNA was sequenced (Illumina NovaSeq; 150 bp PE), reads were mapped to the GT1 genome, and differential expression was analyzed with DESeq2 ($|\log_2 FC| \geq 1$; FDR < 0.01).

**(A) Principal-component analysis (PCA).** PC1 (40%) cleanly separates treated from control samples, whereas PC2 (28%) differentiates time points, indicating a robust, time-dependent transcriptional shift upon TgENT1 knockdown.

**(B) Heat-map of the 50 most variable genes.** Z-scored expression values highlight a concerted up-regulation of purine- and nitrogen-metabolism genes (reds) and down-regulation of cytoskeletal / motility genes (blues) that intensifies from Day 1 to Day 2.

**(C) Volcano plots of differentially expressed genes.** Pink, up-regulated; blue, down-regulated; grey, non-significant. The magnitude and number of responsive genes expand markedly by Day 2. The complete list of genes and fold change is presented of **supplemental table 4**.

**(D) Overlap of DE genes between time points.** Venn diagrams show 96 genes up-regulated at both Day 1 and Day 2, and 58 genes consistently down-regulated, underscoring a core TgENT1-dependent regulon that is sustained and amplified over time.

**(E) Functional enrichment analysis.** Dot-plot of the top Gene Ontology / KEGG terms (size = gene count; color = $-\log_{10}$FDR). Up-regulated sets are dominated by **purine metabolism**, **nitrogen-compound metabolism**, and **cyano-/taurine-derivative pathways**, whereas down-regulated sets are enriched for **microtubule-based movement** and related processes, consistent with a shift from proliferation to metabolic stress adaptation.

**<u>Supplemental material:</u>**

**Supplemental Figure 1: Multiple sequence alignment of equilibrative nucleoside transporter (ENT/AT) homologs highlighting conservation across apicomplexan,**

**kinetoplastid, and human sequences, with human ENT1 transmembrane topology reference.**

Shown are *Toxoplasma gondii* TgAT1 (TGME49_244440), TgENT1 (TGME49_288540), TgENT2 (TGME49_500147), TgENT3 (TGME49_233130); *Plasmodium falciparum* PfENT1; *Cryptosporidium parvum* CpNT1; *Leishmania major* LmNT1; *Saccharomyces cerevisiae* FUN26; *Arabidopsis thaliana* ENT1; *Naegleria fowleri* NT1-like; and *Mus musculus* ENT1, and human ENT1. Sequence labels list protein shorthand (species in parentheses omitted for concision here) followed by aligned residue span (e.g., "/1–696"). Sequences were aligned with MAFFT L-INS-i; no manual internal residue edits were introduced (only removal of obvious trailing low-complexity overhangs where noted). Amino acids are colored by physicochemical class (ClustalX scheme) to facilitate rapid visual inspection of conserved motifs. Histogram bars beneath each block depict position-specific conservation (gold = high conservation / strongly similar physicochemical class; gray = variable) and gap frequency (black). Black horizontal rectangles above the alignment mark the experimentally validated transmembrane helices of human ENT1 (SLC29A1), provided as a structural topology reference against which parasite, plant, protozoan, and kinetoplastid homologs can be compared.

**Supplemental Figure 2: Intracellular replication (parasites per vacuole) and multi-cycle lytic growth (plaque numbers) of parental and ENT mutant strains. (A)** Distribution of vacuole sizes (stacked categories: 2, 4, 8, 16, 32, 64, 128 parasites/vacuole) at 2 days (left) and 3 days (right) post-infection under standard tachyzoite conditions for parental ME49Δku80, ΔTgAT1, complemented

ΔTgAT1::TgAT1-myc, ΔTgENT2, ΔTgENT3, complemented ΔTgENT3::TgENT3-ty, and the double mutant ΔTgAT1ΔTgENT3. For each strain and time point at least 100 vacuoles were scored per biological replicate (n=3 independent infections). Bars show mean percentage ± SEM of total vacuoles; categories sum to ~100%. No significant differences in overall replication distribution between strains were detected by two-way ANOVA (factors: strain, vacuole size category) strain comparisons at each time point). **(B)** Plaque formation after 10 days of continuous lytic growth in HFF monolayers (crystal violet staining). Bars indicate mean plaque number ± SEM (n=3 independent plates per strain; each point = one plate). One-way ANOVA revealed no significant difference among strains ($p>0.05$). Data indicate that deletion (or complementation) of individual ENTs or combined loss of TgAT1 and TgENT3 does not measurably impair tachyzoite intracellular replication over 72 h nor cumulative multi-cycle growth under these assay conditions.

**Supplementary Figure S3. Reduced cyst size in ΔTgAT1 and ΔTgAT1ΔTgENT3 relative to parental and single ENT mutants. (A)** Quantification of cyst diameters (median ± Standard Error of the Mean) for in vitro differentiated bradyzoites (alkaline pH, Day 3) of the indicated strains: parental ME49Δku80, ΔTgAT1, complemented ΔTgAT1::TgAT1-myc, ΔTgENT2, ΔTgENT3, complemented ΔTgENT3::TgENT3-ty, and the double mutant ΔTgAT1ΔTgENT3. Each point represents the mean of one biological replicate (n=3 independent differentiations); ≥150 DBA+ cysts were measured per strain per replicate using an automated ImageJ macro**.** One-way ANOVA multiple comparisons test detected significantly smaller cysts in ΔTgAT1 and ΔTgAT1ΔTgENT3

compared with parental and respective complemented strains (**** $p<0.0001$); "ns" = not significant. **(B)** Representative high-magnification images of DBA-stained cysts (magenta in merge; direct grayscale shown in second column) from each strain at Day 3. Columns: transmitted light (Phase), DBA (cyst wall), anti-Tg (pan-parasite antibody marking internal bradyzoites), DAPI (host and parasite nuclei), and merged composite (DBA green, anti-Tg magenta, DAPI blue). Complemented lines restore cyst sizes and wall morphology towards parental phenotype. Scale bars: 10 µm. Images acquired under identical exposure and processing settings across strains. Data support a delay/reduction in cyst maturation rather than a complete differentiation block in transporter mutants.

**Supplementary Figure S4. In vivo brain cyst burden and morphology after 30 days of infection with parental and ENT mutant strains. (A)** Total brain cyst counts (cysts per mouse) at 30 days post intraperitoneal infection (250 tachyzoites) with the indicated strains: parental ME49Δku80, ΔTgAT1, complemented ΔTgAT1::TgAT1-myc, ΔTgENT2, ΔTgENT3, complemented ΔTgENT3::TgENT3-ty, and the double mutant ΔTgAT1ΔTgENT3. Each point = one mouse brain; bars show mean ± SEM. Two independent experiments were performed (4 male C57BL/6J mice per strain per experiment; symbols pooled after confirming no experiment–strain interaction by two-way ANOVA). No significant difference in total cyst burden among strains (one-way ANOVA, $p>0.05$). **(B)** Mean cyst diameter (µm) ± Standard Error of the Mean (SEM) for DBA-positive cysts from the same brains (≥50 cysts measured per strain across mice; automated ImageJ pipeline with uniform thresholding). ΔTgENT3 and ΔTgAT1ΔTgENT3

display significantly smaller cysts relative to parental and their respective complemented lines (one-way ANOVA with Tukey's multiple comparisons). *p<0.05, **p<0.01, ns = not significant.

**(C)** Representative fluorescence images of individual brain cysts stained with Dolichos biflorus agglutinin (DBA; cyst wall, green in merge), anti-Toxoplasma (pan-parasite antibody, magenta), and DAPI (nuclei, blue). Smaller, less fully expanded cysts are evident in ΔTgENT3 and most pronounced in the double mutant. Complementation ( TgENT3-ty1) restores cyst morphology toward parental appearance. Images acquired under identical acquisition settings; Scale bar: 10 µm.

**Supplementary Figure S5. PCR validation of TgENT knockouts, double knockout, and epitope/complementation lines.**

**(A) Diagnostic PCR across endogenous loci.** Genomic DNA from eight parasite lines (lane order, left to right: 1 ΔTgENT2; 2 ΔTgAT1ΔTgENT3; 3 parental ME49; 4 ΔTgENT3; 5 ΔTgAT1; 6 ΔTgENT3::TgENT3-Ty1; 7 ΔTgAT1::AT1-myc; 8 $H_2O$ control) was amplified with primer pairs specific for GRA17 (loading control) (P7/P8), TgENT1 (P9/P10), TgENT2 (P11/P12), TgENT3 (P13/P14) or TgAT1 (P15/P16), as indicated above each gel strip. Absence of the wild-type amplicon (or size-shift where a repair cassette was inserted) confirms successful disruption, whereas parent and complemented strains retain the expected band.

**(B) Verification of selectable-marker and complementation inserts.** Individual PCRs using primers flanking the repair junctions demonstrate correct integration of the chloramphenicol-acetyl-transferase (CAT) cassette into ΔTgAT1 (top)

(P17/P18) and ΔTgENT3 (fourth panel) (P19/P20), of the AT1-myc (P21/P22) and ENT3-Ty (P23/P24) complementation cassettes into their respective loci (second and third panels), and of a DHFR cassette into the ΔTgAT1ΔTgENT3 line (bottom) (P25/P26). Lane order for each gel: 1 edited line; 2 parental ME49; 3 water control. The PCR product was Sanger-sequenced as confirmation.

**(C) Integration of the mAID-HA tag at the TgENT1 locus.** PCR with locus-specific primers yields the diagnostic HA-junction product exclusively in the TgENT1-mAID-HA strain (lane 1) but not in RH-TIR1 (lane 2) or water control (lane 3), confirming single-locus tagging (P27/P28).

Molecular-weight ladders are shown in the first lane of each gel; expected band sizes are indicated by yellow arrowheads. Together, these assays verify the correct genetic architecture of all strains used in this study.

**Supplemental Table 1:** Oligo list detailing ssDNA sequences used for cloning, genotyping, qPCR, and guide RNAs.

**Supplemental Table 2:** Full DNA sequences of our plasmids used for creation of mutant strains.

**Supplemental Table 3:** List of antibodies used for immunofluorescence detection.

**Supplemental Table 4:** Differentiation expression analyzes of TgENT1 knockdown 24- and 48-hours post-infection.

## Methods

**Parasite Maintenance:** *Toxoplasma gondii* tachyzoites, ME49 and RH strains, were propagated in human foreskin fibroblasts (HS27; ATCC CRL-1634) at 37 °C in DMEM supplemented with 10 % FBS, 100 U/ml penicillin, and 100 µg/ml streptomycin. Cells and parasite lines were tested for mycoplasma monthly using a PCR test (Boca Scientific).

**Plasmid Construction:** Final sequences are listed in **Supplementary Table 2**. PCRs employed Q5 High-Fidelity (long fragments) or Taq DNA polymerase (routine amplifications). Amplicons and vector backbones were assembled with Gibson Assembly (NEB) unless noted.

- **ΔTgENT3 donor** – synthetic plasmid (GenScript).
- **ΔTgENT3::TgENT3-Ty1 donor** – 23-DD plasmid digested with BglI. Synthetic insert (B1) ordered and inserted (Twist Bioscience).
- **ΔTgAT1 donor** – ΔTgENT3 donor digested with AvrII/NotI (insert) and SpeI/AflII (backbone); 5′ and 3′ TgAT1 homology arms amplified with P1/P2 and P3/P4.
- **TgENT3-DHFR-KO donor** – DHFR cassette (Addgene #80329) amplified with P5/P6 and inserted into ΔTgENT3 backbone (NotI/EcoRV).
- **mAID-HA-TgENT1 donor** – synthetic plasmid (GenScript).
- **ΔTgAT1::TgAT1-myc donor** – 24-DD plasmid digested with BssHI/ScaI. Synthetic inserts (B2 and B3) ordered and inserted (Twist Bioscience).
- **ΔTgENT2** – ΔTgENT3 donor digested with AflII/SnaBI. Synthetic insert (B4) ordered and inserted (Twist Bioscience).

- **Guide RNA plasmids** – pSS013 vector (Addgene) was BsaI-linearised; annealed IDT oligos were inserted by Gibson Assembly, transformed into *E. coli* DH5α, sequence-verified, and prepared with GeneJET Maxi kits.

**Genomic Editing and Transfection:** Knock-outs, knock-ins, and mAID tagging were generated with dual-guide CRISPR–Cas9 as described (voltage 1500 V, 0.1 ms, two pulses; BTX ECM™ 830, 4-mm cuvette). Parasites harvested from confluent T25 flasks were washed once in cytomix (120 mM KCl, 0.15 mM $CaCl_2$, 10 mM $K_2HPO_4/KH_2PO_4$ pH 7.6, 25 mM HEPES, 2 mM EGTA, 5 mM $MgCl_2$). Electroporation mixtures contained 50 µg linearized donor DNA and 25 µg of each sgRNA plasmid in 400 µl cytomix. Parasites were immediately added to fresh HS27 monolayers. Drug selection began 24 h post-transfection (40 µM chloramphenicol or 3 µM pyrimethamine). Drug-resistant populations were single-cell-sorted (or cloned by limiting dilution), expanded, and validated by diagnostic PCR, Western blot, and immunofluorescence (primer sets P7–P28; see Supplementary Table 2).

**AlphaFold Modeling:** Predicted protein structures were retrieved from the AlphaFold Protein Structure Database (AlphaFold DB) using their UniProt accession code. These predicted structures were aligned with human ENT1 (PDBID: 6OB7) using PyMOL version 3.1.4.1 (Schrodinger). Root Mean Square Deviation (RMSD) of each transporter relative to human ENT1 was calculated using PyMOL. Atomic measurements of pore width were also performed in PyMOL. As shown using HsENT1 in **Fig. 1C**, pore width was measured across the widest and narrowest points (yellow and red dashed lines). TgENT1, TgENT2, TgENT3, and TgAT1 pores were measured in the same manner.

**Immunofluorescence Assay:** Cells were fixed in 3.7% formaldehyde for 20 minutes, washed twice with 1x PBS, blocked and permeabilized with 3% BSA and 0.2% Triton X-100 for 2 hours at room temperature (or, alternatively, overnight at 4°C). Primary antibodies were diluted 1:500 (unless otherwise stated in Supplemental Table 3) in blocking/permeabilization solution and incubated for 1 hour at room temperature (or overnight at 4°C). Cells were washed twice with 1x PBS, secondary antibodies were applied at 1:500 dilution (DAPI at 1:200) in blocking/permeabilization solution for one hour at room temperature, washed three times for 5 minutes, and glass coverslips were mounted and sealed.

**Pearson and Manders' colocalization coefficients:** Pearson's *r* and Manders' coefficients assess spatial overlap between two fluorescence signals after background removal. Pearson's correlation coefficient (*r*) measures the linear proportionality of intensities on a pixel-by-pixel basis (−1 to 1), whereas Manders' M1 and M2 report the fraction of fluorophore A (or B) signal that coincides with the other channel independent of intensity proportionality. Colocalization was quantified in raw 16-bit TIFF images using Fiji (ImageJ) Coloc2. After identical acquisition (no saturation; sequential capture to avoid bleed-through), images were opened without gamma adjustment, a uniform rolling-ball background subtraction was applied to both channels, and no nonlinear filtering or manual thresholding was performed. Reported values in the manuscript are the averages of 50 vacuoles per condition pooled from three independent biological experiments.

**Bradyzoite *in vitro* differentiation:** The *in vitro* differentiation was performed as previously [34]. Confluent HS27 fibroblast monolayers on glass coverslips were infected with freshly egressed tachyzoites (MOI ≈1; 2 h invasion + gentle wash; total pre-induction incubation 4 h). Cultures were then shifted to pre-warmed alkaline induction medium (RPMI 1640 supplemented with 1% heat-inactivated FBS, 50 mM HEPES, pH 8.20 ± 0.05 at 37 °C) and incubated in ambient air (≈0.04% $CO_2$) in a humidified chamber (no external $CO_2$) to maintain pH ≥8.0. Induction medium was replaced every 24 h with freshly adjusted medium; pH was spot-checked at each change. After 2-, 3-, or 7-days post-infection, coverslips were fixed (4% paraformaldehyde/PBS, 20 min), permeabilized (0.2% Triton X-100), and dual-stained with rabbit anti-*Toxoplasma* antibody (Thermo Fisher; 1:500) to delineate vacuoles and Dolichos biflorus agglutinin (DBA; 2–5 µg/ml) to label the cyst wall. A vacuole was scored "differentiated" if ≥75% of its perimeter showed a continuous DBA rim. For each condition ≥100 vacuoles per coverslip were scored blindly (≥3 biological replicates).

**Tachyzoite Intracellular Growth and Plaque Assays:** Confluent HS27 (human foreskin fibroblast) monolayers on glass coverslips were infected with each *T. gondii* strain at an MOI yielding mostly isolated vacuoles (typically MOI 0.5–1.0) in standard pH 7.4 medium (DMEM + 10% FBS, 5% $CO_2$). After allowing invasion for 2 h at 37 °C, extracellular parasites were removed by two PBS washes and fresh medium was added. At the indicated post-infection time point in each experiment, cells were fixed in 4% paraformaldehyde (15 min), permeabilized (0.1% Triton X-100, 10 min), and

blocked (3% BSA/PBS, 30 min). Parasites were labeled with anti-*Toxoplasma* (followed by Alexa Fluor–conjugated secondary antibody). For each biological replicate, 100 intact, non-overlapping parasitophorous vacuoles were randomly selected using a Cytation 7 imager (Agilent) under consistent exposure settings, and the number of tachyzoites per vacuole was recorded. Three biological replicates were performed per experiment. Vacuoles at the edge of fields, obviously disrupted, or with uncertain boundaries were excluded during counting.

For **plaque assays**, confluent HS27 monolayers in 6-well plates were infected with 1,000 of freshly egressed tachyzoites in 2 mL of complete medium. At endpoint, monolayers were fixed in 100% ethanol (10 min) and stained with 0.1% crystal violet (in 20% methanol) for 15–20 min, rinsed, and air-dried. Plaques (zones of host cell clearance) were imaged, counted manually and plaque areas were measured after background subtraction and uniform threshold application. At least three biological replicates (independent parasite preparations on different days) per strain were analyzed. Statistical analysis used one-way ANOVA with appropriate multiple comparison correction. **Quality controls.** Parasite viability and inoculum accuracy were confirmed by counting extracellular tachyzoites with a hemocytometer.

**RNA extraction, mRNA sequencing and transcriptomics analyses:** Total RNA was extracted from *T. gondii* infected cells using the GeneJET RNA Purification Kit (Thermo Fisher Scientific) according to the manufacturer's protocol. RNA quality and concentration were confirmed, and poly(A)-selected mRNA libraries were subsequently prepared by Novogene. Libraries were sequenced on an Illumina NovaSeq X Plus

platform, generating 150-bp paired-end reads. All experiments were performed in biological triplicate, and the resulting data are publicly available in the NCBI Sequence Read Archive under BioProject accession PRJNA1247533. Reads were adapter- and quality-trimmed with Cutadapt, mapped to the reference genome using STAR in splice-aware mode, and uniquely aligned reads were summarized to gene-level counts with featureCounts. Differential expression was then evaluated in R with DESeq2, which applied median-of-ratios normalization, negative-binomial GLM fitting, and Benjamini–Hochberg correction to identify significantly regulated genes.

**Immunofluorescence Assay for PLVAC Morphology:** PLVAC morphology was assessed 36 h post-infection in TgENT1 AID-HA tachyzoites ± IAA. Parasites were mechanically released (27-g needle) from host cells and immediately inoculated onto fresh confluent HS27 monolayers for a 30-min invasion pulse (37 °C). Cultures were fixed in 4% paraformaldehyde (20 min, RT) and stained with primary anti-TgCPL antibody (PLVAC marker) followed by appropriate fluorophore-conjugated secondary antibodies and DAPI. Imaging was performed under identical acquisition settings across conditions. For each condition, the cross-sectional area of the first 50 TgCPL-positive PLVAC puncta associated with intracellular parasites was quantified (Fiji) in each of three biological replicates (n = 50 vacuoles/condition). Areas were compared by t-test.

**Animal experiments**

All animal work was approved by the University of Vermont IACUC (protocol PROTO202100038) and performed in accordance with institutional guidelines. Mice

were housed under a 12 h light/12 h dark cycle with daily health monitoring that began one week before infection and continued until study end; animals were euthanized if predefined humane endpoints were met.

Two independent experiments were conducted. In each, four adult male CBA/J mice (The Jackson Laboratory) per parasite strain received an intraperitoneal inoculation of 250 freshly-egressed tachyzoites suspended in 200 µl sterile PBS. At 30 days post-infection (dpi), mice were euthanized following IACUC protocol, and whole cortices were promptly harvested for downstream analyses.

Brain immunofluorescence was conducted as previously reported [37]. Briefly, the tissue was homogenized using serial needles passing through 18-, 20-, and 22-gauge needles, pelleted at 1000xg for 5 minutes, and fixed with 3.7% formaldehyde for 20 minutes. Pellets were washed twice with 1x PBS, blocked overnight in 1% BSA and 0.2% Triton X-100 in 1x PBS, primary antibodies diluted 1:500 were incubated overnight, washed twice with 1x PBS, secondary antibodies (1:500 dilution) and DAPI were added for 1 hour, washed twice with 1x PBS, and imaged using a microscope.

Cyst stained with DBA were wet mounted onto coverslips and scanned for DBA using a Cytation 7 imager (Agilent). 50 randomly found cysts per sample were measured and recorded using Agilent BioTek Gen5 software.

**qPCR**

RNA was extracted from freshly lysed tachyzoites using the GeneJet RNA Purification Kit. Complementary DNA (cDNA) was subsequently synthesized employing the Maxima

H Minus First Strand cDNA Synthesis Kit. Quantitative PCR (qPCR) reactions were then set up with primers Q1 – Q8 using the PowerSYBR Green PCR Master Mix.

**Statistical Analysis**

GraphPad Prism 9 was used for all statistics. Data are mean ± SEM of ≥3 independent experiments. Group differences were analyzed by one-way ANOVA or unpaired two-tailed Student's *t*-test (as indicated). $P < 0.05$ (**), 0.01 (**), and 0.0001 (*****) were considered significant.

**Acknowledgments**

This research was supported by a research grant from National Institutes of Health (P20 GM125498). We thank Dr. Harry de Koning for helpful discussions.

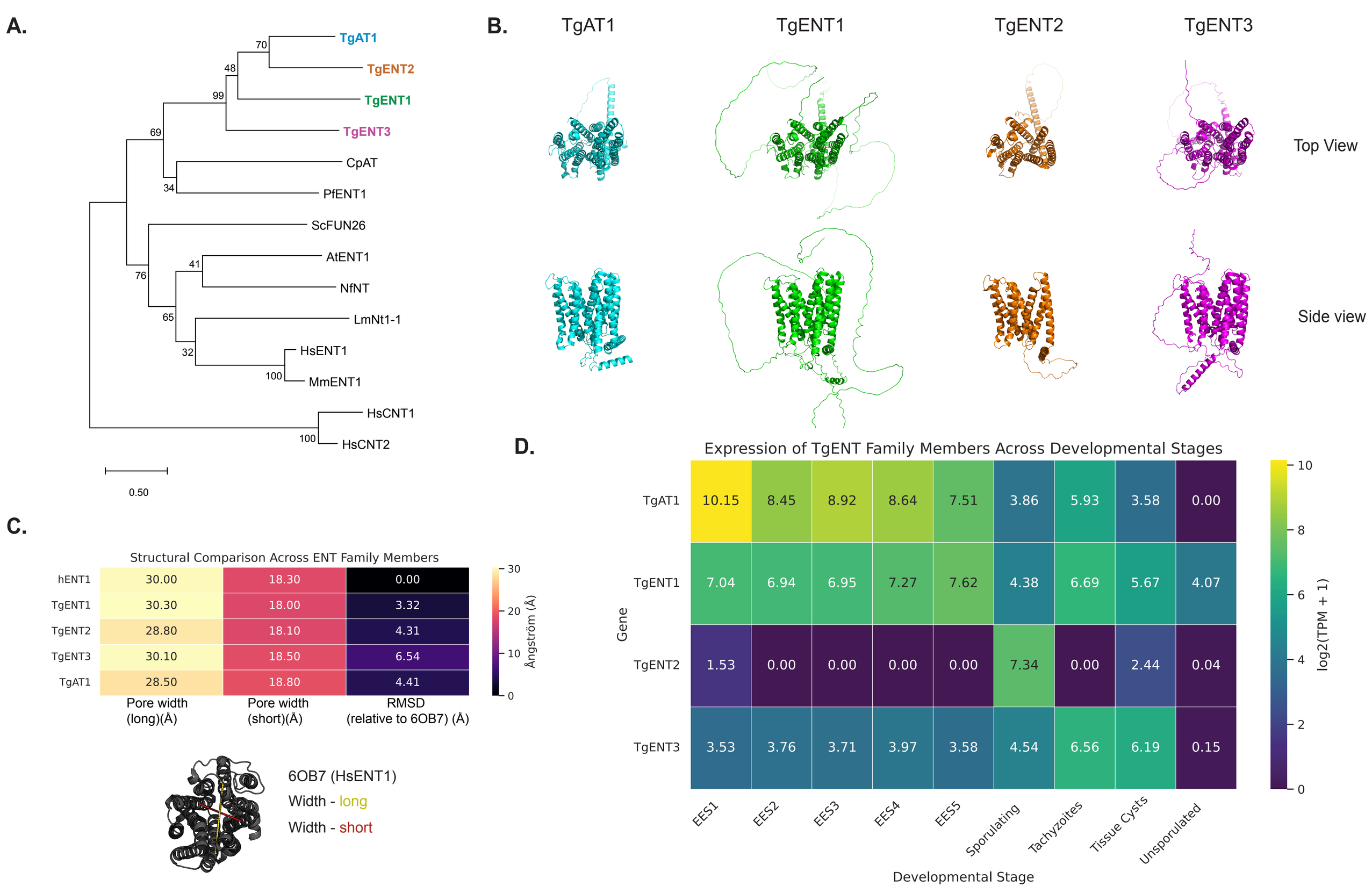
A.
TgAT1
TgENT2
TgENT1
TgENT3
CpAT
PfENT1
ScFUN26
AtENT1
NfNT
LmNt1-1
HsENT1
MmENT1
HsCNT1
HsCNT2
70
48
99
69
34
76
41
65
32
100
100
0.50
B.
TgAT1
TgENT1
TgENT2
TgENT3
Top View
Side view
C.
Structural Comparison Across ENT Family Members
hENT1 30.00 18.30 0.00
TgENT1 30.30 18.00 3.32
TgENT2 28.80 18.10 4.31
TgENT3 30.10 18.50 6.54
TgAT1 28.50 18.80 4.41
Pore width (long)(Å)
Pore width (short)(Å)
RMSD (relative to 6OB7) (Å)
Ångström (Å)
30
20
10
0
6OB7 (HsENT1)
Width - long
Width - short
D.
Expression of TgENT Family Members Across Developmental Stages
Gene
TgAT1 10.15 8.45 8.92 8.64 7.51 3.86 5.93 3.58 0.00
TgENT1 7.04 6.94 6.95 7.27 7.62 4.38 6.69 5.67 4.07
TgENT2 1.53 0.00 0.00 0.00 0.00 7.34 0.00 2.44 0.04
TgENT3 3.53 3.76 3.71 3.97 3.58 4.54 6.56 6.19 0.15
EES1
EES2
EES3
EES4
EES5
Sporulating
Tachyzoites
Tissue Cysts
Unsporulated
Developmental Stage
log2(TPM + 1)
10
8
6
4
2
0

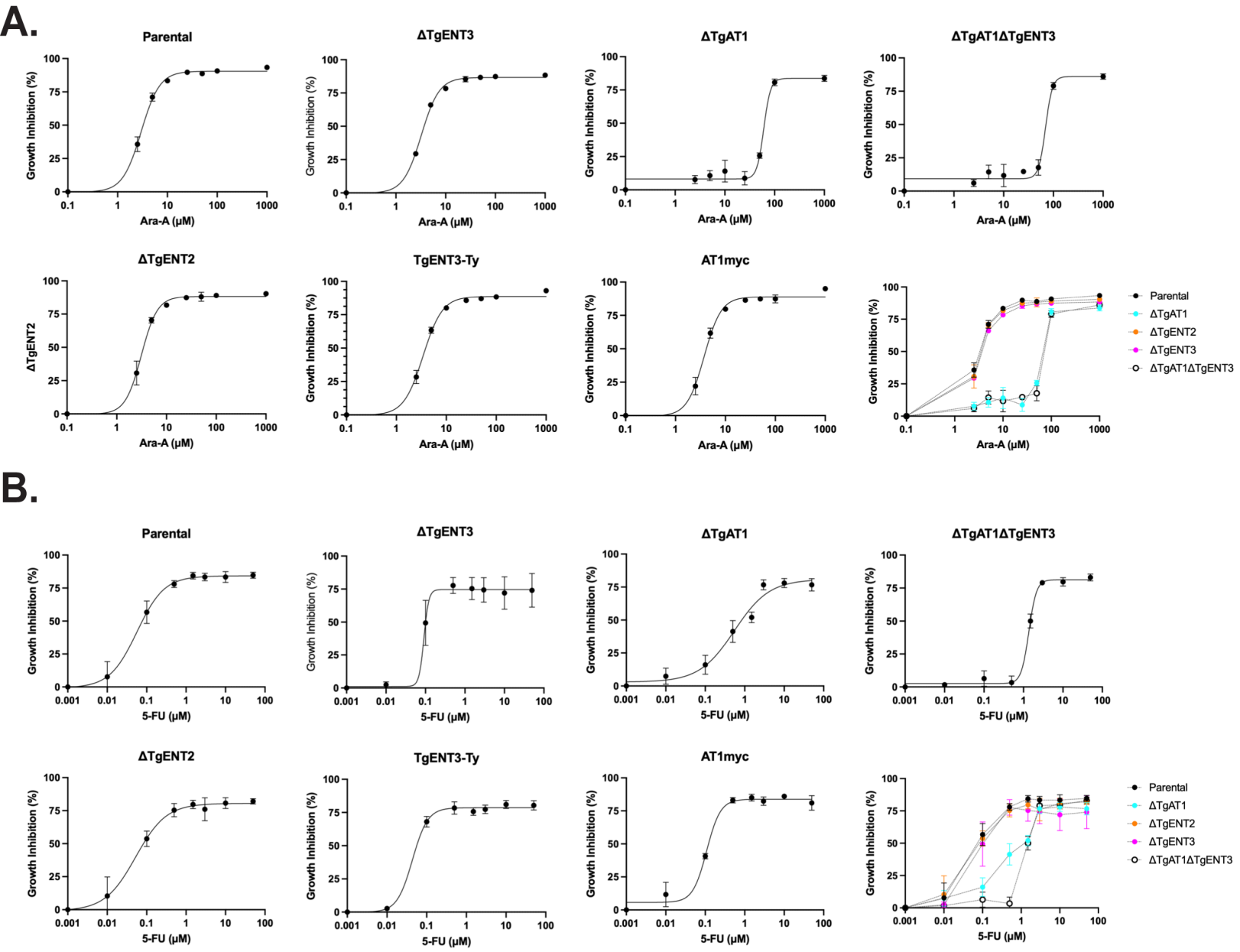
A.
Parental
ΔTgENT3
ΔTgAT1
ΔTgAT1ΔTgENT3
ΔTgENT2
TgENT3-Ty
AT1myc
Growth Inhibition (%)
ΔTgENT2
Ara-A (μM)
Parental
ΔTgAT1
ΔTgENT2
ΔTgENT3
ΔTgAT1ΔTgENT3
B.
5-FU (μM)

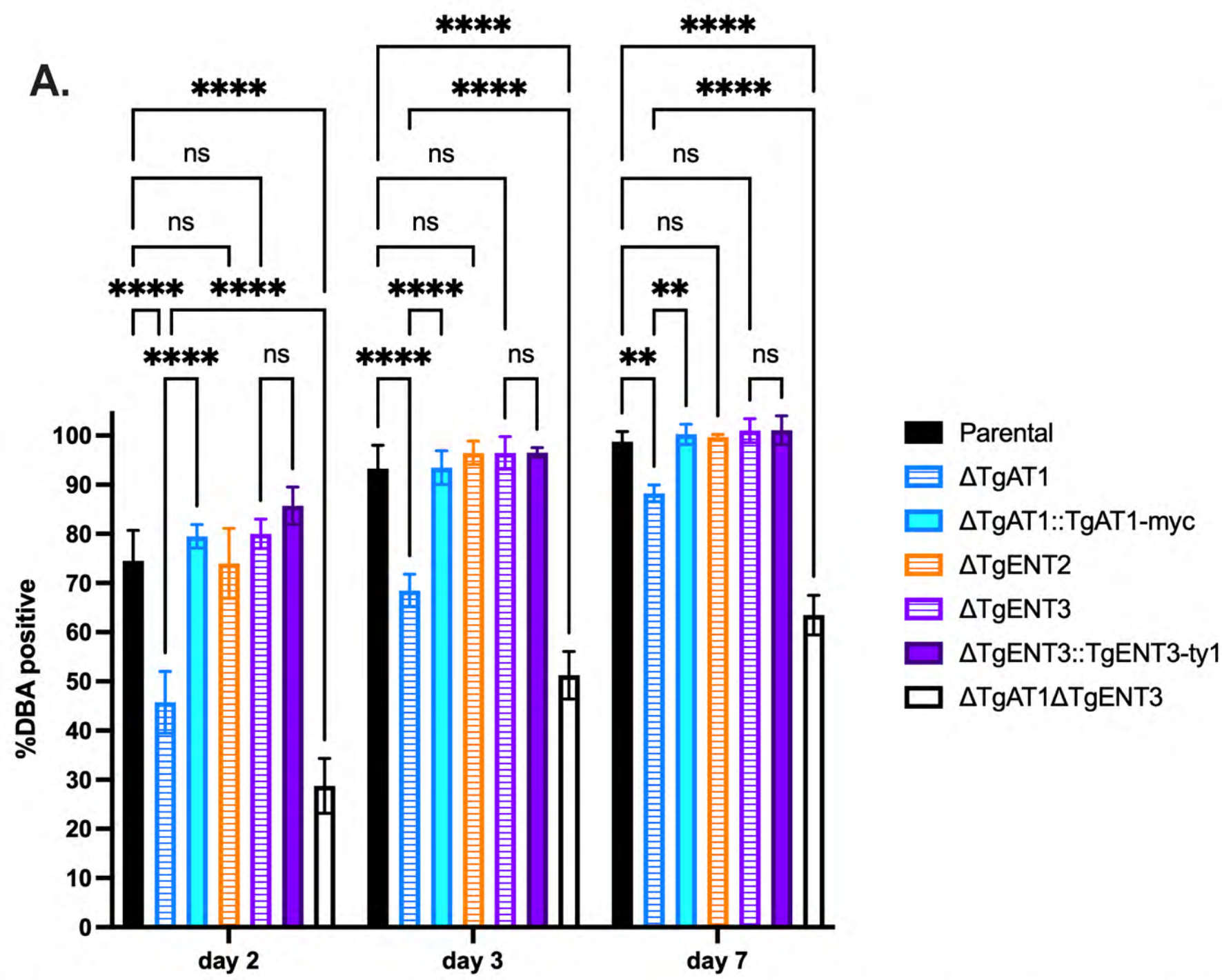
A.
%DBA positive
day 2
day 3
day 7
****
ns
**
Parental
ΔTgAT1
ΔTgAT1::TgAT1-myc
ΔTgENT2
ΔTgENT3
ΔTgENT3::TgENT3-ty1
ΔTgAT1ΔTgENT3

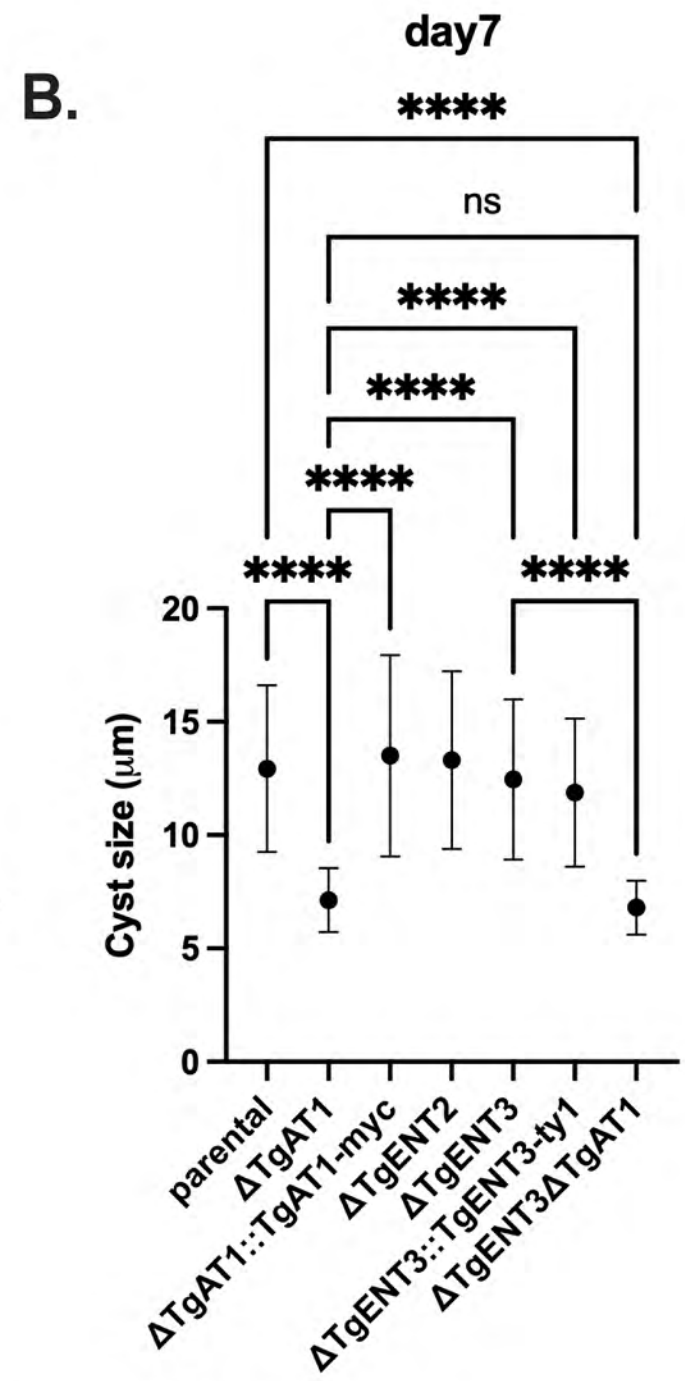
B.
day7
Cyst size (μm)
****
ns
parental
ΔTgAT1
ΔTgAT1::TgAT1-myc
ΔTgENT2
ΔTgENT3
ΔTgENT3::TgENT3-ty1
ΔTgENT3ΔTgAT1

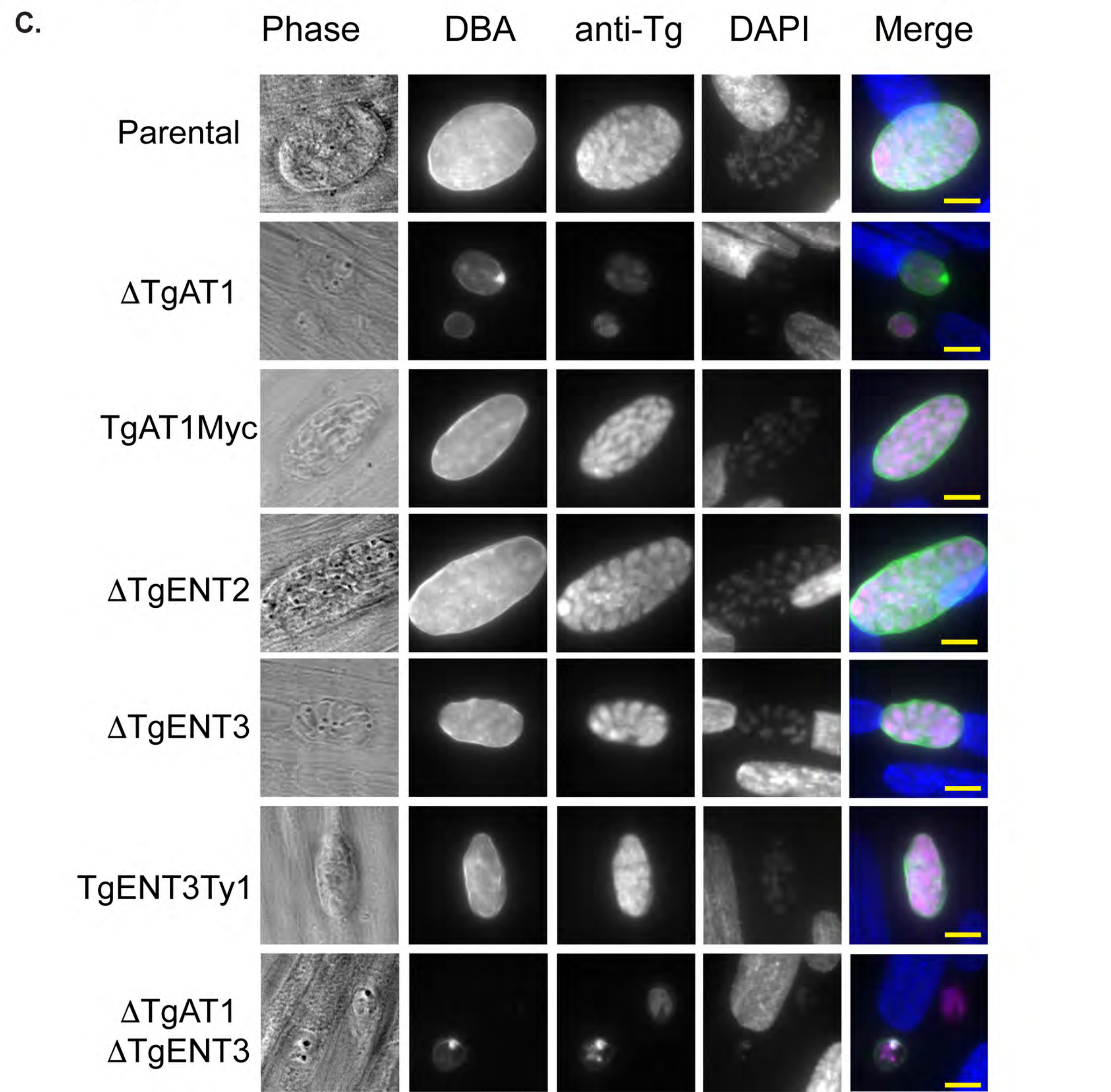
C.
Phase
DBA
anti-Tg
DAPI
Merge
Parental
ΔTgAT1
TgAT1Myc
ΔTgENT2
ΔTgENT3
TgENT3Ty1
ΔTgAT1
ΔTgENT3

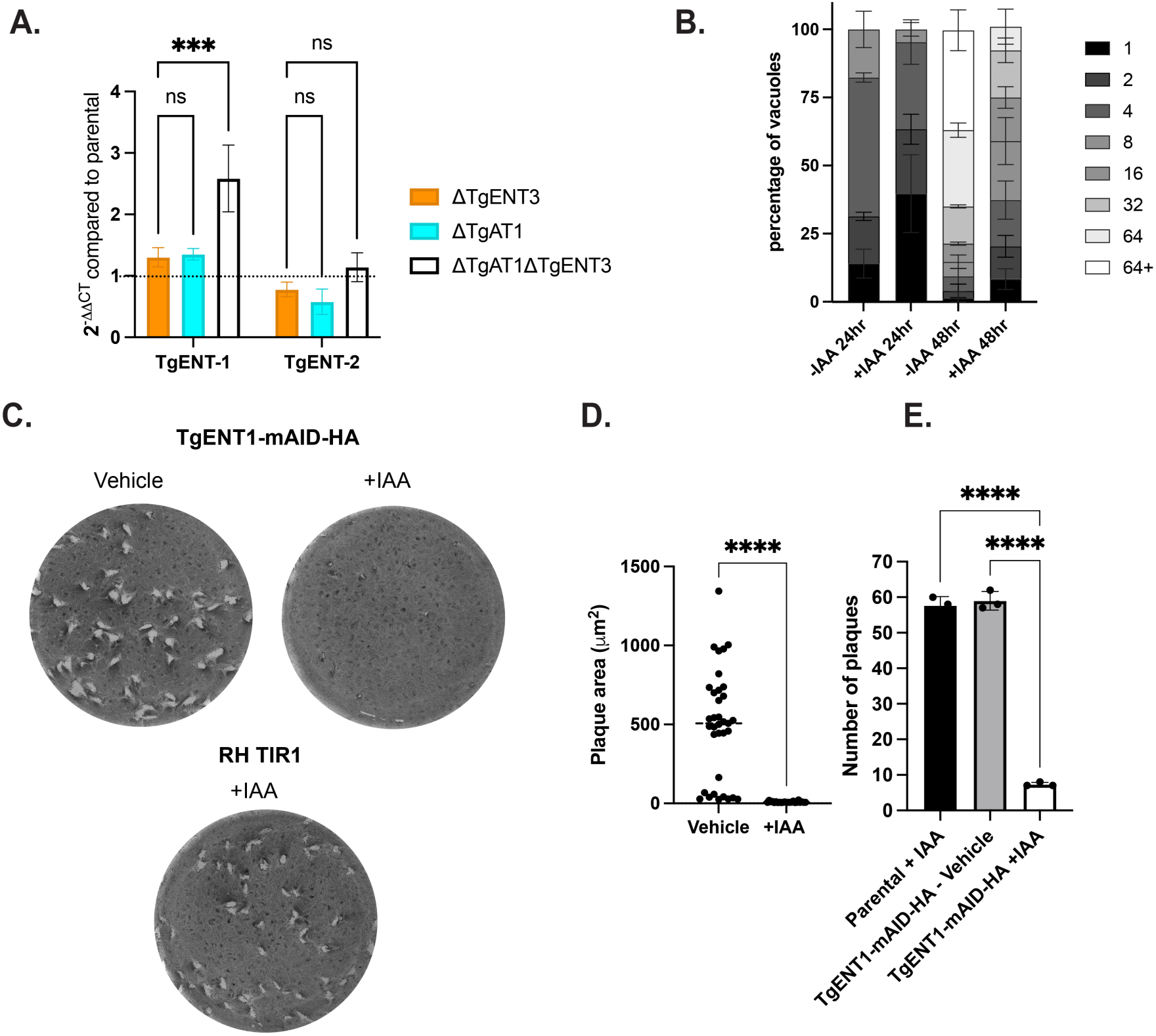
A.
***
ns
ns
ns
$2^{-\Delta\Delta CT}$ compared to parental
4
3
2
1
0
TgENT-1
TgENT-2
ΔTgENT3
ΔTgAT1
ΔTgAT1ΔTgENT3
B.
percentage of vacuoles
100
75
50
25
0
-IAA 24hr
+IAA 24hr
-IAA 48hr
+IAA 48hr
1
2
4
8
16
32
64
64+
C.
TgENT1-mAID-HA
Vehicle
+IAA
RH TIR1
+IAA
D.
****
Plaque area (μm²)
1500
1000
500
0
Vehicle
+IAA
E.
****
****
Number of plaques
70
60
50
40
30
20
10
0
Parental + IAA
TgENT1-mAID-HA - Vehicle
TgENT1-mAID-HA +IAA

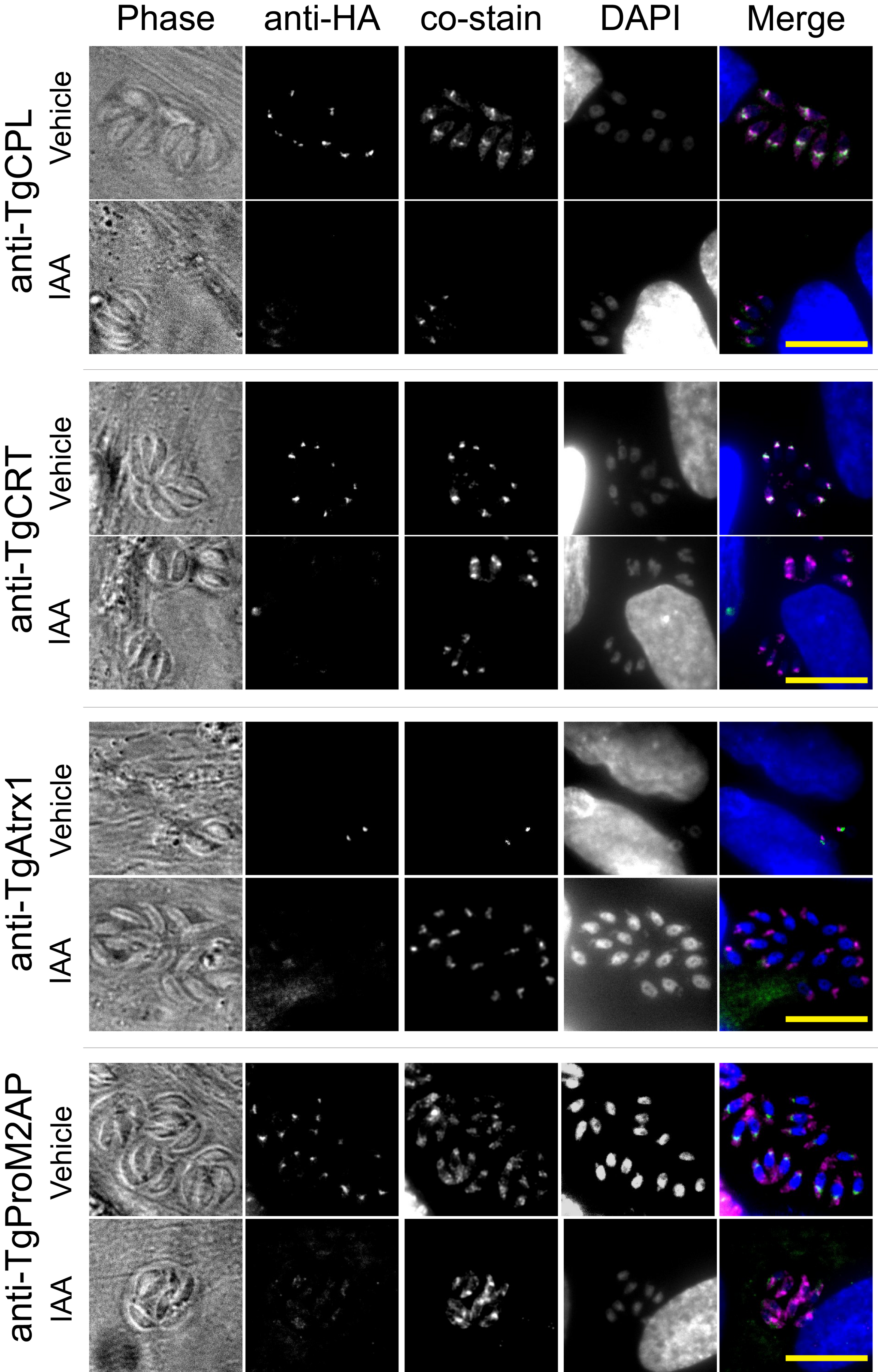
Phase
anti-HA
co-stain
DAPI
Merge
anti-TgCPL
Vehicle
IAA
anti-TgCRT
Vehicle
IAA
anti-TgAtrx1
Vehicle
IAA
anti-TgProM2AP
Vehicle
IAA

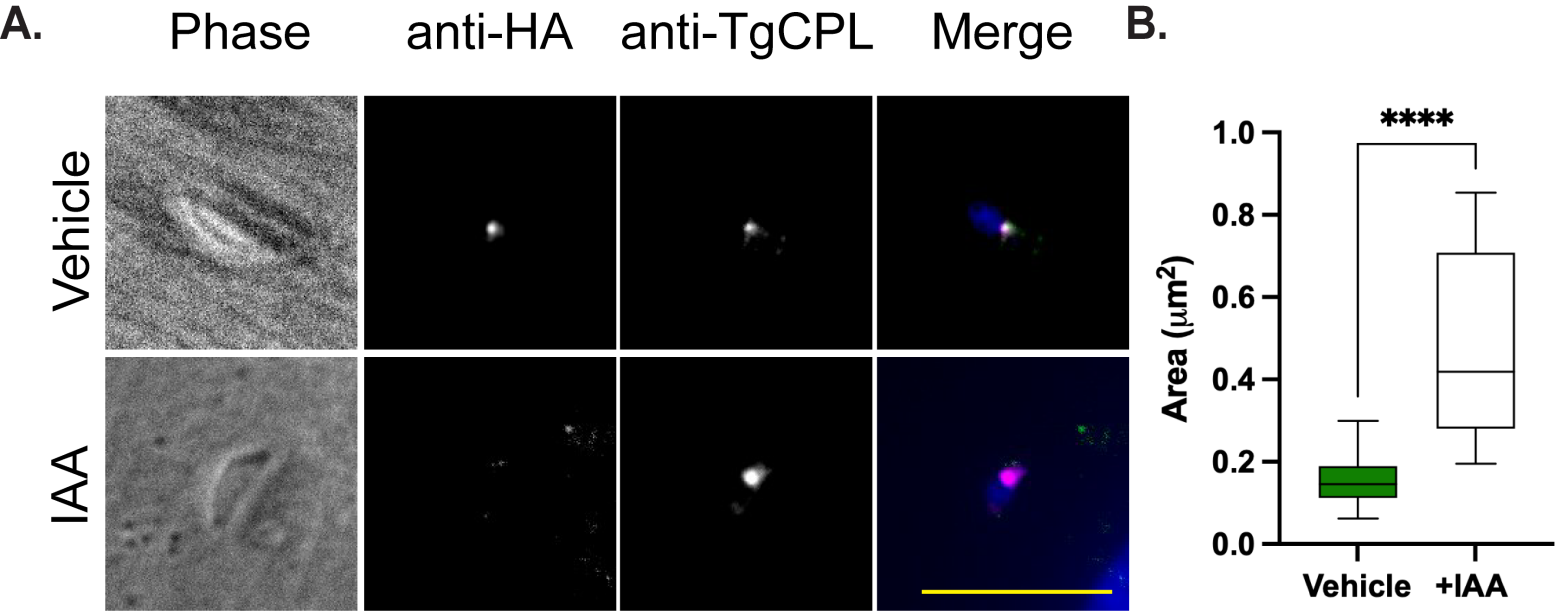
A.
Phase
anti-HA
anti-TgCPL
Merge
Vehicle
IAA
B.
****
1.0
0.8
0.6
0.4
0.2
0.0
Area (μm²)
Vehicle
+IAA

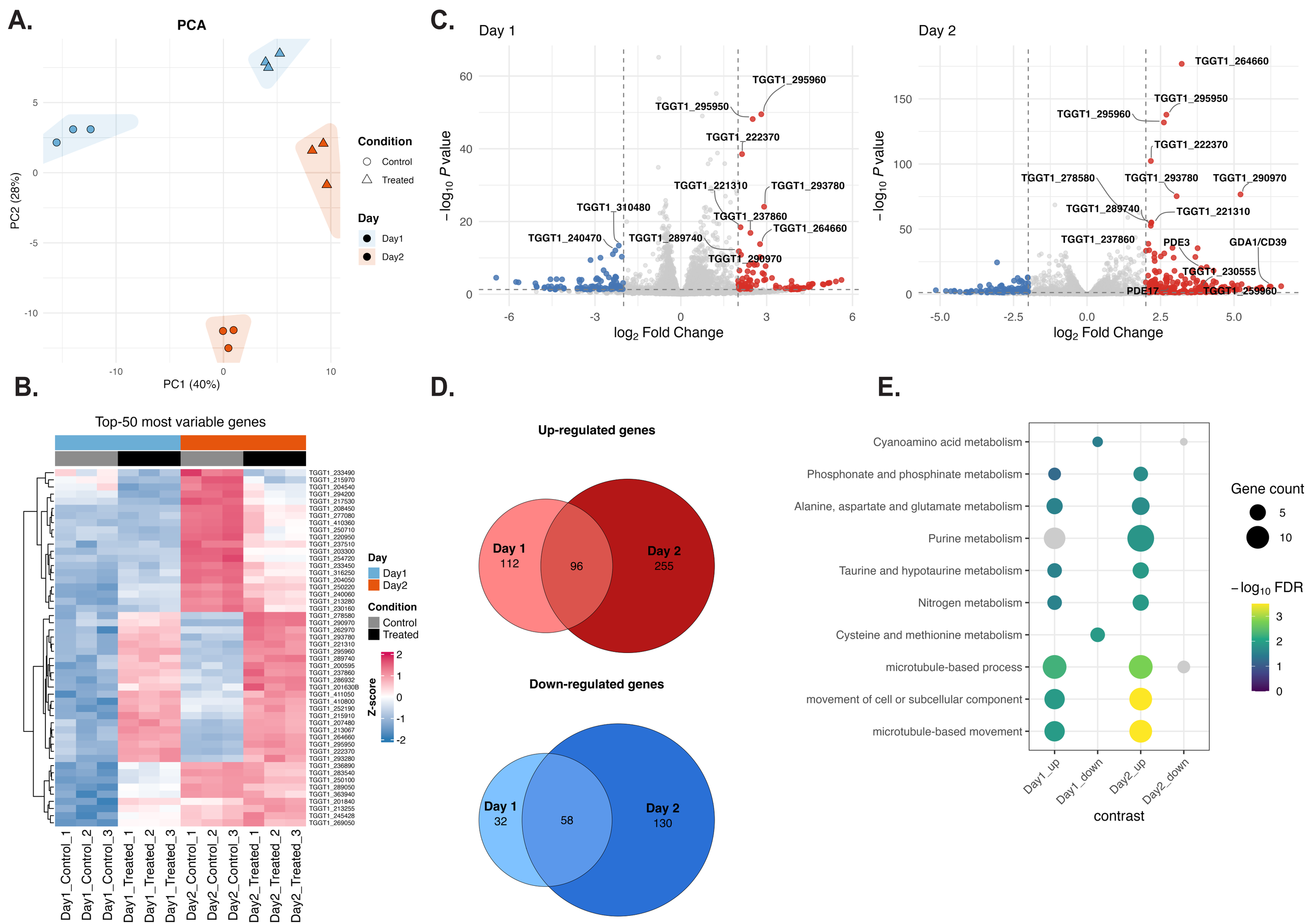
A.
PCA
PC2 (28%)
PC1 (40%)
Condition
Control
Treated
Day
Day1
Day2
B.
Top-50 most variable genes
Day
Day1
Day2
Condition
Control
Treated
Z-score
Day1_Control_1
Day1_Control_2
Day1_Control_3
Day1_Treated_1
Day1_Treated_2
Day1_Treated_3
Day2_Control_1
Day2_Control_2
Day2_Control_3
Day2_Treated_1
Day2_Treated_2
Day2_Treated_3
C.
Day 1
Day 2
$-\log_{10}$ P value
$\log_2$ Fold Change
TGGT1_295960
TGGT1_295950
TGGT1_222370
TGGT1_221310
TGGT1_293780
TGGT1_310480
TGGT1_237860
TGGT1_264660
TGGT1_240470
TGGT1_289740
TGGT1_290970
TGGT1_278580
TGGT1_289740
TGGT1_237860
PDE3
GDA1/CD39
TGGT1_230555
PDE17
TGGT1_259960
D.
Up-regulated genes
Day 1
112
96
Day 2
255
Down-regulated genes
Day 1
32
58
Day 2
130
E.
Cyanoamino acid metabolism
Phosphonate and phosphinate metabolism
Alanine, aspartate and glutamate metabolism
Purine metabolism
Taurine and hypotaurine metabolism
Nitrogen metabolism
Cysteine and methionine metabolism
microtubule-based process
movement of cell or subcellular component
microtubule-based movement
Day1_up
Day1_down
Day2_up
Day2_down
contrast
Gene count
$-\log_{10}$ FDR